

PONTIFICIA UNIVERSIDAD CATÓLICA DEL PERÚ

FACULTAD DE CIENCIAS E INGENIERÍA



**ACOUSTIC NONLINEARITY PARAMETER ESTIMATION USING THE
DEPLETION METHOD AND FULL ANGULAR SPATIAL COMPOUNDING FOR
ENHANCED ULTRASOUND IMAGING IN BREAST COMPUTATIONAL MODELS**

Tesis para obtener el título profesional de Ingeniero Electrónico

AUTOR:

Erik David Miranda Zárate

ASESOR:

Andres Leonel Coila Pacompia


Lima, 2026

Informe de Similitud

Yo, **Andres Leonel Coila Pacompia**, docente de la Facultad de **Ciencias e Ingeniería** de la Pontificia Universidad Católica del Perú, asesor de la tesis titulada **Acoustic nonlinearity parameter estimation using the depletion method and full angular spatial compounding for enhanced ultrasound imaging in breast computational models**, del autor **Erik David Miranda Zárate**, dejo constancia de lo siguiente:

- El mencionado documento tiene un índice de puntuación de similitud de 21%. Así lo consigna el reporte de similitud emitido por el software *Turnitin* el **04/02/2026**.
- He revisado con detalle dicho reporte y la Tesis, y no se advierte indicios de plagio.
- Las citas a otros autores y sus respectivas referencias cumplen con las pautas académicas.

Lugar y fecha: **Lima, 04 de febrero de 2026**

Apellidos y nombres del asesor: Coila Pacompia, Andres Leonel	
DNI: 43575870	Firma: 
ORCID: https://orcid.org/0000-0002-2924-3888	



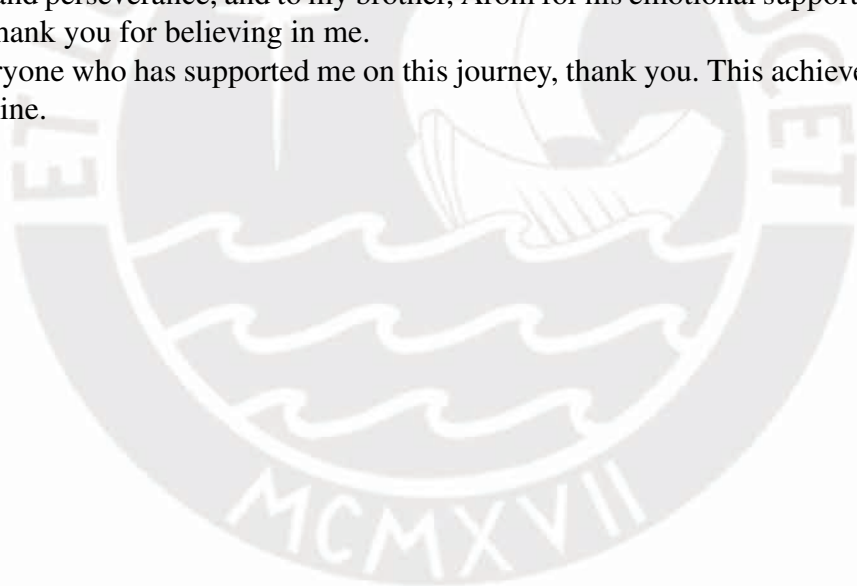
Acknowledgments

Completing this thesis has been a challenging but rewarding journey and would not have been possible without the guidance, support and encouragement of my family and friends, and the blessings and grace of God.

First, I express my gratitude to my advisor, Dr. Andres Leonel Coila Pacompia, for his support, feedback, and guidance throughout the course of this research. His expertise and mentorship have been instrumental in shaping this work and my growth as a researcher.

On a personal note, I am indebted to my family for their unconditional love, understanding, and encouragement. To my parents, Edmundo and Milagros, for instilling in me the value of education and perseverance, and to my brother, Arom for his emotional support during moments of doubt, thank you for believing in me.

To everyone who has supported me on this journey, thank you. This achievement is as much yours as mine.



Resumen

Las anomalías del tejido mamario constituyen una preocupación significativa para la salud pública, resaltando la urgencia de desarrollar técnicas avanzadas de imágenes para facilitar un diagnóstico temprano. Por consiguiente, el ultrasonido mamario resulta beneficioso pues proporciona información sobre tejidos blandos a través de parámetros acústicos. En este contexto, el parámetro de no linealidad acústica (B/A) es relevante, dado que los tejidos mamarios anómalos tienden a exhibir valores de B/A menores en comparación con un tejido sano. Este trabajo de tesis presenta una nueva metodología para mejorar la adquisición de imágenes por ultrasonido mamario mediante la integración del marco de trabajo del método de reducción de la amplitud de la banda fundamental, el cual estima valores acumulativos del B/A que posteriormente se transforman en estimaciones locales mediante la formulación de un problema inverso estabilizado con regularización de variación total (TV, por sus siglas en inglés), con un promediado espacial angular completo (FASC, por sus siglas en inglés), una técnica que mejora la calidad de la imagen al aprovechar múltiples ángulos de adquisición. A partir de esta combinación, se supera las limitaciones del método sin FASC al mejorar la resolución espacial, disminuir el ruido e incrementar la claridad de la imagen.

Para evaluar el rendimiento del método propuesto, se efectuaron simulaciones numéricas del tejido mamario con un valor de B/A uniforme de 10, e inclusiones con valores de 5.5, 6.5 y 8.0. Se generaron mapas de B/A para comparar el enfoque FASC con imágenes de vista única, inicialmente sin regularización y luego con regularización TV. El método combinado FASC+TV demostró una reducción de ruido superior, una delimitación más precisa y una disminución de varianza. Estos resultados destacan el potencial del método para mejorar la caracterización de tejidos al proporcionar mapas de B/A más precisos.

Abstract

Breast tissue abnormalities constitute a major public health concern, highlighting the urgency for advanced imaging techniques to facilitate early diagnosis. Consequently, breast ultrasound is beneficial in providing unique soft tissue information via acoustic parameters. Among them, the acoustic nonlinearity parameter (B/A) is especially informative, given that abnormal breast tissues tend to have lower B/A values in comparison to healthy tissue. This research presents a novel methodology to enhance breast ultrasound imaging by integrating the framework of the depletion method (DM), which estimates cumulative B/A values later converted into local estimates via an inverse problem stabilized with total variation (TV) regularization, with full angular spatial compounding (FASC), a technique that improves image quality by leveraging multiple viewing angles. Through this integration, the approach aims to address the limitations of conventional methods by enhancing spatial resolution, reducing noise, and improving image clarity.

To evaluate the performance of the proposed model, numerous numerical simulations were performed utilizing a background B/A value of 10, and inclusions with values of 5.5, 6.5 and 8.0. B/A maps were computed to compare the FASC approach with single-view imaging, initially without regularization and then with TV regularization. The combined FASC+TV method demonstrated superior noise reduction, clearer delineation, and lower variance. These results highlight the method's potential to improve tissue characterization by providing accurate B/A maps.

Content

Introduction	1
I Quantitative ultrasound in breast imaging	2
1.1 Problematic	2
1.2 QUS parameters description	4
1.2.1 Acoustic nonlinearity parameter	4
1.2.2 Backscatter coefficient	6
1.2.3 Attenuation coefficient	6
1.3 Full angular spatial compounding	7
1.4 <i>B/A</i> methods description	8
1.4.1 Finite amplitude method (FAM)	8
1.5 Justification and importance	10
1.6 Hypothesis	11
1.7 Objectives	11
1.7.1 General objective	11
1.7.2 Specific objectives	11
II Concepts, advanced techniques, and tools for quantitative ultrasound in breast imaging	12
2.1 The wave equation	12
2.1.1 Acoustic waves: 3D	13
2.1.2 Plane waves	13
2.2 Ultrasound imaging	14
2.2.1 Systems	14
2.2.2 Transducers	15
2.2.3 Steering and focusing	15
2.3 Acoustic nonlinearity theory	16
2.3.1 Depletion method	17
2.3.2 Inversion approach	20
2.4 Datasets	21
2.4.1 k-Wave toolbox	21
2.4.2 Experiment description	21
2.5 <i>B/A</i> maps reconstruction	22

2.5.1	Filtering	22
2.5.2	Implementation	24
2.6	Full angular spatial compounding	25
2.7	Evaluation metrics	27
III Simulation framework and <i>B/A</i> estimation pipeline using depletion and FASC techniques		28
3.1	Procedure sequence	28
3.2	Proposed model	29
3.3	Simulation setup	30
3.3.1	Water interface	30
3.3.2	Numerical phantom design	31
3.3.3	Transducer specifications	33
3.3.4	k-Wave toolbox	33
3.4	Dataset construction	34
3.5	RF data acquisition	35
3.5.1	RF signal generation	35
3.5.2	RF data collection process	35
3.6	RF data process	35
3.6.1	Depletion method implementation	35
3.6.2	Inversion approach	38
3.6.3	Full angular spatial compounding	39
IV Quantitative evaluation of <i>B/A</i> imaging: Impact fo FASC and TV regularization		40
4.1	Computer simulation recap	40
4.1.1	Dataset versions: V1star	41
4.1.2	Dataset versions: V1a & V1b	41
4.1.3	Dataset versions: V2a & V2b	42
4.1.4	Dataset versions: V3a & V3b	43
4.2	Impact of the number of viewing angles on reconstruction performance	44
4.2.1	Dataset versions: V1star	45
4.2.2	Dataset versions: V1a & V1b	47
4.2.3	Dataset versions: V3a & V3b	52
4.3	Impact of the regularization parameter μ on reconstruction performance	56
4.3.1	Dataset versions: V1a & V1b	56
4.4	<i>B/A</i> estimation comparison	59
4.4.1	Dataset versions: V1star	59
4.4.2	Dataset versions: V1a & V1b	60
4.4.3	Dataset versions: V3a & V3b	62
Conclusions		64

Recommendations

65

Bibliography

66

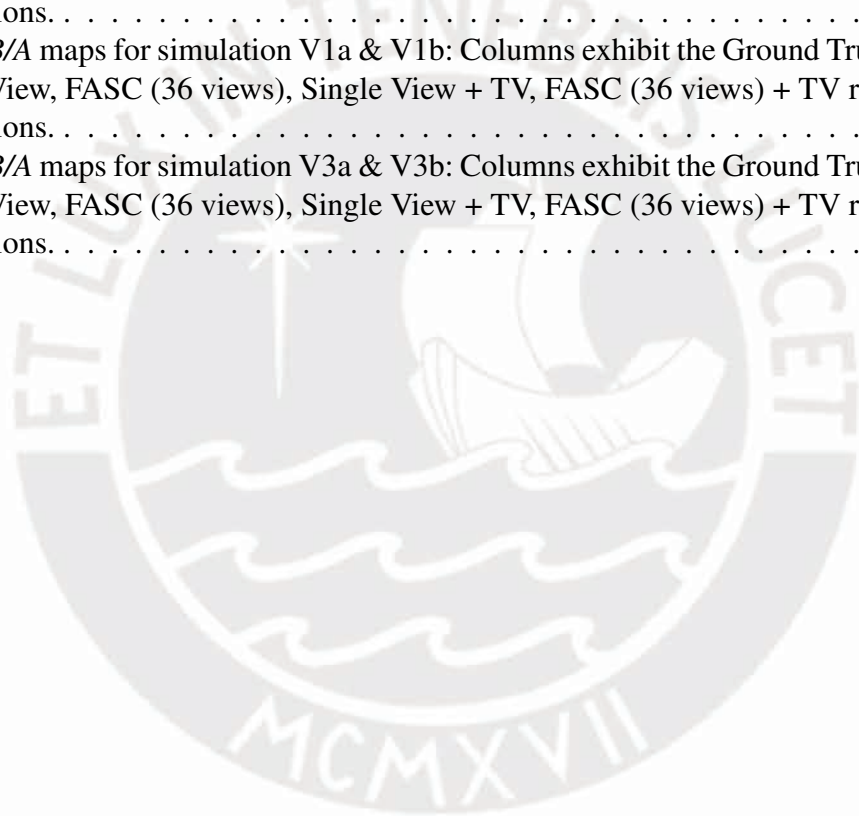


List of Figures

2.1	Block diagram highlighting a conventional US imaging system, adapted from [59].	14
2.2	a) Linear waveform and its spectrum centered at 2.25MHz. b) Severely distorted waveform and its spectrum containing a series of harmonics centered at a multiple of the original frequency. Adapted from [59].	17
2.3	(a) B-mode display (no visible contrast of the inclusion). (b) Ground truth <i>B/A</i> map with the values assigned to the background and the inclusion. Adapted from [55].	22
2.4	Band-pass filter [3.5-6.5] MHz at $f_0 = 5$ MHz and an order of 200.	23
2.5	Comparison between the low-pressure (80 kPa) original and filtered data at $f_0 = 5$ MHz.	23
2.6	(a) Depletion method image. (b) Inversion approach of (a). Adapted from [55].	24
2.7	[On both phantoms] (a), (d): Single view B-mode output. (b), (e): Single view attenuation coefficient displays. (c), (f): FASC attenuation maps, adapted from [49].	26
2.8	FASC illustration: US transducer rotating around the breast during data acquisition, adapted from [63].	26
3.1	Block diagram of the procedure sequence.	29
3.2	Proposed model configuration for breast tissue: A phantom, along with its inclusion being laterally displaced a specified rotational angle θ . Initial reference angle for the rotation ($\theta' = 0^\circ$). L: transducer-phantom distance. D: phantom diameter. d: inclusion diameter.	30
3.3	Breast anthropometric measurements diagram, adapted from [69].	32
3.4	[B-mode image]: Sample low-pressure (80 kPa) $\theta = 90^\circ$	36
3.5	Comparison between the sample low-pressure (80 kPa) Pre-filtered and Post-filtered middle RF signal in the frequency domain, $\theta = 90^\circ$	37
4.1	[Dataset V1star, $\theta = 90^\circ$] (a) <i>B/A</i> map, (b) Attenuation Coeff. map, (c) Density map	41
4.2	[Dataset V1a-b, $\theta = 90^\circ$] (a) <i>B/A</i> map, (b) Attenuation Coeff. map, (c) Density map	42
4.3	[Dataset V2a-b, $\theta = 90^\circ$] (a) <i>B/A</i> map, (b) Attenuation Coeff. map, (c) Density map	43

4.4	[Dataset V3a-b, $\theta = 90^\circ$] (a) <i>B/A</i> map, (b) Attenuation Coeff. map, (c) Density map	44
4.5	[Dataset V1star, $\theta = 90^\circ$] <i>B/A</i> maps of a star-cross shaped inclusion. Results are shown for both single view and FASC reconstructions with 4, 12 and 36 views. The transducer is adjacent to the phantom.	45
4.6	[Dataset V1star]: (a) Mean \pm SD. The horizontal dashed lines represent the ground truth values for the background (red), and inclusion M (blue). (b) Standard Deviation.	46
4.7	[Dataset V1star]: (a) CNR. (b) NRMSE.	46
4.8	[Dataset V1a, $\theta = 90^\circ$] <i>B/A</i> maps of a single circular inclusion. Results are shown for both single view and FASC reconstructions with 4, 12 and 36 views. The transducer is adjacent to the phantom.	47
4.9	[Dataset V1a]: (a) Mean \pm SD. The horizontal dashed lines represent the ground truth values for the background (red), and inclusion M (blue). (b) Standard Deviation.	48
4.10	[Dataset V1a]: (a) CNR. (b) NRMSE.	48
4.11	[Dataset V1a1-a4, $\theta = 90^\circ$] <i>B/A</i> maps of a single circular inclusion. Results are shown for both single view and FASC reconstructions with 4, 12 and 36 views. (a) $d = 0.875$ cm, (b) $d = 0.750$ cm, (c) $d = 0.625$ cm, and (d) $d = 0.500$ cm. The transducer is adjacent to the phantom.	49
4.12	[Dataset V1a1-a4]: NRMSE (a) $d = 0.875$ cm, (b) $d = 0.750$ cm, (c) $d = 0.625$ cm, and (d) $d = 0.500$ cm.	50
4.13	[Dataset V1b, $\theta = 90^\circ$] <i>B/A</i> maps of a single circular inclusion. Results are shown for both single view and FASC reconstructions with 4, 12 and 36 views. The transducer is positioned 1 cm away from the phantom.	50
4.14	[Dataset V1b]: (a) Mean \pm SD. The horizontal dashed lines represent the ground truth values for the background (red), and inclusion M (blue). (b) Standard Deviation.	51
4.15	[Dataset V1b]: (a) CNR. (b) NRMSE.	51
4.16	[Dataset V3a, $\theta = 90^\circ$] <i>B/A</i> maps of a single circular inclusion. Results are shown for both single view and FASC reconstructions with 4, 12 and 36 views. The transducer is adjacent to the phantom.	52
4.17	[Dataset V3a]: (a) Mean \pm SD. The horizontal dashed lines represent the ground truth values for the background (red) and inclusions M (blue), N (cyan), and P (green). (b) Standard Deviation.	53
4.18	[Dataset V3a]: (a) CNR. (b) NRMSE.	53
4.19	[Dataset V3b, $\theta = 90^\circ$] <i>B/A</i> maps of a single circular inclusion. Results are shown for both single view and FASC reconstructions with 4, 12 and 36 views. The transducer is positioned 1 cm away from the phantom.	54
4.20	[Dataset V3b]: (a) Mean \pm SD. The horizontal dashed lines represent the ground truth values for the background (red) and inclusions M (blue), N (cyan), and P (green). (b) Standard Deviation.	55

4.21 [Dataset V3b]: (a) CNR. (b) NRMSE.	55
4.22 [Dataset V1a]: (a) Mean \pm SD. The horizontal dashed lines represent the ground truth values for the background (red), and inclusion M (blue). (b) Standard Deviation.	56
4.23 [Dataset V1a]: (a) CNR. (b) NRMSE.	57
4.24 [Dataset V1b]: (a) Mean \pm SD. The horizontal dashed lines represent the ground truth values for the background (red), and inclusion M (blue). (b) Standard Deviation.	57
4.25 [Dataset V1b]: (a) CNR. (b) NRMSE.	58
4.26 <i>B/A</i> maps for simulation V1star: Columns exhibit the Ground Truth, Single View, FASC (36 views), Single View + TV, FASC (36 views) + TV reconstructions.	59
4.27 <i>B/A</i> maps for simulation V1a & V1b: Columns exhibit the Ground Truth, Single View, FASC (36 views), Single View + TV, FASC (36 views) + TV reconstructions.	60
4.28 <i>B/A</i> maps for simulation V3a & V3b: Columns exhibit the Ground Truth, Single View, FASC (36 views), Single View + TV, FASC (36 views) + TV reconstructions.	62



List of Tables

1.1	Acoustic nonlinearity parameters for various mediums.	5
1.2	Implemented FAMs β imaging echo mode approaches.	9
2.1	Acoustic properties for various biological tissues	13
3.1	Acoustic properties of water used as an interface in ultrasound simulations . . .	31
3.2	Comparison of IR and R between countries	31
3.3	Acoustic properties of the numerical phantoms and their inclusions used in simulations	33
3.4	Transducer configuration specifications used in simulations	33
3.5	Hardware and software specifications for simulation environment	34
3.6	Key characteristics for the dataset construction	34
4.1	Statistics for <i>B/A</i> maps of Simulation V1star	60
4.2	Statistics for <i>B/A</i> maps of Simulation V1a	61
4.3	Statistics for <i>B/A</i> maps of Simulation V1b	61
4.4	Statistics for <i>B/A</i> maps of Simulation V3a	63
4.5	Statistics for <i>B/A</i> maps of Simulation V3b	63

Introduction

Breast abnormalities are a common reason women seek medical imaging. Although mammography is a common screening tool, it struggles with dense breast tissue; ultrasound imaging is better for soft tissue evaluation. Conventional ultrasound lacks the specificity to accurately characterize breast abnormalities. Quantitative ultrasound (QUS) techniques aim to overcome these limitations by extracting numerical biomarkers that reflect the acoustic properties of tissues. Among these parameters, the acoustic nonlinearity parameter (B/A) is particularly promising, as its values differ significantly between tissue types and pathological states. However, estimating local B/A values is challenging due to noise sensitivity and low spatial clearance.

This thesis proposes a novel technique that integrates the Depletion method (DM) framework, which uses dual-pressure levels along with an inversion problem regularized with Total variation (TV) to estimate the B/A parameter with Full angular spatial compounding (FASC), which combines information acquired from multiple angles, to improve spatial coherence and noise reduction. The structure of this thesis is organized as follows. Chapter 1 presents the clinical motivation, limitations of conventional B/A estimation, and key QUS parameters. Chapter 2 provides a theoretical background. Chapter 3 the implementation of the proposed framework, and Chapter 4 presents a quantitative evaluation, highlighting the improvements over single-view imaging and discussing key findings.

The results of this thesis were presented at the 2025 IEEE International Ultrasonics Symposium (IUS) [1].

Chapter I

Quantitative ultrasound in breast imaging

This chapter begins by outlining the problematic. Then, the QUS parameters, such as the B/A , the backscatter coefficient (BSC), and the attenuation coefficient (AC) are described. Moreover, the FASC is addressed followed by an explanation of the the DM for QUS estimation. Finally, the thesis's justification, hypothesis, and objectives are highlighted.

1.1. Problematic

Women often seek imaging services due to noticeable breast abnormalities [2], which exhibit a broad spectrum in terms of their characteristics and severity. These range from benign conditions like fibroadenomas [3] and cysts [4] to more serious issues including infections [5], inflammations [6], and precancerous and cancerous conditions [7].

Across the world, breast cancer constitutes the most commonly diagnosed cancer in women and is the second leading cause of cancer-related deaths among them [7,8]. This condition begins as breast cells multiply without control, forming a tumor. The standard screening techniques for breast cancer involve clinical evaluations, physical self-examinations, and mammography [9].

Mammography is a specialized imaging method that employs low-level X-rays to produce detailed images of the breast. However, the primary challenge with mammography is that the structures are far more uniform in composition and density than those in bone or chest X-rays. Additionally, there is a significant need to reduce radiation exposure [10]. Furthermore, the procedure can be uncomfortable, the discomfort stems from the need to compress the breast between two plates to obtain clear images.

Breast ultrasound (US) has emerged as a crucial diagnostic modality that complements mammography [11], due to its widespread and cost-effective availability and ability to provide unique soft tissue information. US becomes particularly handy when dealing with highly dense breasts due to the reduced sensitivity of mammography [9]. Currently, several ultrasound imaging methods are used, including the standard B-mode ultrasonography. Techniques such as harmonic imaging and compound imaging enhance image contrast and resolution. Color Doppler is applied to assess lesion vascularization, yet it remains uncertain whether it distinguishes malignant from benign lesions [11]. While these methods offer clinically important information, emerging QUS provides substantial data valuable for medical diagnosis using numerical acoustic parameters [12], which can assess specific tissue properties.

For instance, the BSC has been used for breast tissue characterization. Numerous studies explored its potential, yet quantitative BSC analysis has not been conclusive in differentiating normal and pathological breast tissue [13–15]. Another parameter that holds potential for tissue characterization is the AC. According to Landini et al. [16], the AC can differentiate breast tissues based on their cellular and collagen fiber content, suggesting its feasibility in identifying malignant breast tumors. Nevertheless, tumors lacking productive fibrosis can not be distinguished from fatty tissues. Lastly, the acoustic nonlinearity parameter may be of great assistance since its values vary significantly between different types of tissues and states of disease [17]. Fat tissue has the highest B/A value measured across soft tissues, ranging between

ten and twelve [18, 19]. Since the breast is primarily composed of fat tissue, the B/A parameter holds promise as a valuable measure when accurately estimated.

1.2. QUS parameters description

Quantitative Ultrasound parameters are essential metrics in medical imaging to assess specific tissue properties, providing valuable information about its structure and composition.

1.2.1. Acoustic nonlinearity parameter

Ultrasound waves are composed of compressions and rarefactions that alternate. In linear acoustics, the linear dependence of medium density on pressure is merely an approximation. In reality, the propagation of ultrasound is a nonlinear process. By using the Taylor series expansion, the relationship between pressure and density can be expressed as the adiabatic equation of state:

$$P = P_0 + \rho_0 \left(\frac{\partial P}{\partial \rho} \right)_{0,S} \frac{\rho - \rho_0}{\rho_0} + \frac{\rho_0^2}{2} \left(\frac{\partial^2 P}{\partial \rho^2} \right)_{0,S} \left(\frac{\rho - \rho_0}{\rho_0} \right)^2 + \dots, \quad (1.1)$$

where P and P_0 represent the instantaneous and hydrostatic pressures, respectively. Meanwhile, ρ and ρ_0 correspond the instantaneous and equilibrium densities of the medium [17]. The parameter B/A is determined as the ratio of the second to the first coefficient in the Taylor series expansion of the medium's equation state [20]. High B/A values often indicate greater nonlinearity, which can be associated with variations in tissue and pathological conditions. Table 1.1 summarizes measured B/A values for animal and human soft tissues and water, adapted from [17].

Table 1.1: Acoustic nonlinearity parameters for various mediums.

Medium	B/A	Reference
Water	5.1	[21]
Porcine Liver	7	[22]
	7.2	[23, 24]
	7.3	[25]
Pathological Porcine Liver	[7.4-10.3]	[26, 27]
Porcine Fat	[10.9-11.3]	[18]
	10.8, 10.9	[28]
	10.7	[25]
Porcine Kidney	6.3, 6.9	[28]
Pathological Porcine Kidney	[7.1-8.1]	[29]
Human Liver	6.5	[30]
Pathological Human Liver	[5.7-8.7]	[31]
Human Breast	10.2	[32]
Human Breast Fat	9.2	[30, 33]
Lymphnode in Breast	8.2	[33]
Multiple Myeloma of the Breast	5.6	[30]
		[31]
Adenocarcinoma Metastatic in Breast	6.5	[31]

In summary, the literature indicates that both human and animal fat tissues exhibit significant nonlinearity. Moreover, pathological tissues often possess B/A values that differ from those in healthy tissues. Therefore, accurately estimating the B/A parameter is crucial in assessing tissue characterization in breast tissue.

1.2.2. Backscatter coefficient

The BSC is an intrinsic tissue property and, therefore remains independent of the operator and the imaging system [34]. It delineates the medium's underlying scattering structures [35]. Recently, it has been used to assess organs such as the liver [36], pancreas [37], and breasts [38] in various *in vivo* examinations.

The BSC is estimated by analyzing the frequency domain of the medium's backscattered signals. To achieve this, two modalities are employed to normalize the power spectrum, known as the planar reference method applicable when using single-element transducers [39, 40] and the reference phantom technique that allows the use of clinical array systems [41]. In the first approach, a planar surface with minimal roughness relative to the wavelength is employed. Made from a reflective material near the focal region of the transducer providing a reference signal [34]. Meanwhile, in the reference phantom framework, calibration signals are obtained using a precisely defined reference phantom with known acoustic properties [20].

1.2.3. Attenuation coefficient

The AC describes the losses, such as absorption or scattering which occur as US waves travel through a medium, quantifying the reduction in US wave intensity [42]. This parameter is used for the characterization of both tissue pathologies and general tissue properties [43]. For example, Kuc et al. [44] observed that inflamed livers exhibit lower attenuation coefficients than normal, whereas cirrhotic livers display higher values than healthy ones. In breast tissue, Landini et al. [16] reported that the attenuation coefficient tends to be low for fatty tissue, while high for collagen. Current studies have focused on soft tissues including the liver [45], breast [46] and placenta [47].

Attenuation measurements are highly dependent on the algorithm's accuracy. Current methods are primarily conducted in the frequency domain within a region of interest, including the spectral log difference, the spectral difference, and the hybrid methods [43].

1.3. Full angular spatial compounding

The FASC technique in ultrasound imaging, enhances image quality by acquiring and combining images from multiple viewing angles. For example, in Coila et al. [48] the method involves data acquisition from a range of scanning angles spanning 0° to 360° . This angular coverage is used to estimate the examined tissue's AC and BSC.

The FASC method enhances the quality of AC slope (ACS) maps, crucial for compensating the total attenuation effects during the estimation of BSCs, enabling for more reliable and consistent characterization of tissue properties, particularly in scenarios where a complete angular field of view is accessible such as breast imaging. This method can be approached by moving laterally a single-element transducer over the sample, several times until a full 360° view is completed [49] or by using a transducer arrangement distributed around a 360-degree angle.

1.4. *B/A* methods description

QUS methods significantly enhance the functionality of ultrasound imaging for visualization and quantitative assessment and characterization of different tissue types.

1.4.1. Finite amplitude method (FAM)

The local speed of a US wave is determined by the *B/A* parameter and the excess density at the corresponding space and time. Consequently, the wave distorts as it propagates, leading to the generation of higher harmonics. FAM approaches evaluate the propagated wave to estimate the *B/A* parameter based on the accumulation of nonlinear response. They can be categorized into three groups: techniques based on the shape of the wave, second harmonic and fundamental component. Table 1.2 summarizes implemented FAMs β imaging echo mode approaches, adapted from [17].

Table 1.2: Implemented FAMs β imaging echo mode approaches.

Method	Reference signal	Studied Media	Probe	Reference
2nd Harmonic estimation	Fundamental at two harmonic frequency $2f_0$	Homogeneous bovine liver	Two transducers	[50]
		Homogeneous <i>in vivo</i> human liver	Sector array transducer	[51]
		Homogeneous tissue	Compound piezoelectric transducer	[23]
	Fundamental at f_0	Tissue-mimicking phantom with two layers	Esaote LA332 commercial probe	[52]
	2nd harmonic in reference medium	Two tissue-mimicking phantoms	Clinical probe	[53]
	Fundamental at f_0 and 2nd harmonic in a reference medium	Tissue-mimicking phantom with three layers	Commercial probe	[54]
Depletion	Reference phantom	Tissue-mimicking phantom	L9-4/38 clinical probe	[55]
Variable Amplitude Excitation	Water and ethyl alcohol	Media with different nonlinearities	Single transducer	[56,57]

Depletion method

According to Coila et al. [55], the depletion method is described as a technique used to estimate the B/A of fluid-like media using a dual-energy approach. This method involves modifying the analysis of radio frequency data envelopes from the fundamental band to overcome the limitations observed when the reference phantom and sample medium display distinct AC slopes.

1.5. Justification and importance

This thesis suggests a focused study on improving breast ultrasound imaging through advanced quantitative techniques. This can be obtained by using the Depletion method in [55], which has shown improved performance and accuracy in estimating the B/A parameter compared to previous models, especially in scenarios where the sample and the reference phantom differed in the AC values. Likewise, the FASC technique is particularly effective in contexts where a full angular field of view is accessible, such as breasts. This technique reduces the variance AC and BSC, thereby improving the quality of the ultrasound images [48].

It is intended to integrate the depletion method with the FASC to capitalize on the strengths of both approaches, aiming to enhance image quality and achieve a more precise tissue characterization. Ultimately, the current literature does not possess the synergistic application of these two advanced techniques in any type of soft tissue so this research aims to bridge this gap.

1.6. Hypothesis

The use of the depletion method along with the full angular spatial compounding technique to estimate the B/A significantly enhances the quality and diagnostic capabilities of breast ultrasound imaging compared to traditional ultrasound imaging techniques.

1.7. Objectives

1.7.1. General objective

To develop and validate an approach for estimating the B/A by combining the depletion method with FASC, aiming to enhance the accuracy and quality of ultrasound imaging in computational breast models for improved tissue characterization and diagnostic capabilities.

1.7.2. Specific objectives

1. To simulate numerical phantoms of breast models using the k-Wave toolbox in MATLAB®.
2. To develop and test an integrated approach that combines FASC with the depletion method for estimating the acoustic B/A with data from simulated phantoms.
3. To compare the new method's performance with the depletion method regarding accuracy and precision.

Chapter II

Concepts, advanced techniques, and tools for quantitative ultrasound in breast imaging

This chapter presents theoretical and practical foundations in QUS imaging in breast tissue. It begins by introducing the wave equation as well as 3D acoustic plane waves. Essential components of US systems are outlined, including transducers, steering and focusing mechanisms, and phased array beamforming. Then, highlights the Depletion Method and the inversion-based approach for B/A estimation. The section concludes by presenting the FASC technique and quantitative metrics used for evaluation.

2.1. The wave equation

Acoustic waves travel through a medium by alternating compression and rarefaction. These pressure disturbances are initiated when tissue is compressed and subsequently released. As it repeats in adjacent regions, a propagating wave is created [58].

2.1.1. Acoustic waves: 3D

The physical properties of a material, such as compressibility κ and density ρ , along the fundamental principles of mass and momentum conservation, indicate the presence of acoustic waves; which propagate through the medium at a specific sound speed (SoS) c , expressed as

$$c = \sqrt{\frac{1}{\kappa\rho}}. \quad (2.1)$$

Table 2.1 overviews the c and ρ for various biological tissues, adapted from [58].

Table 2.1: Acoustic properties for various biological tissues

Biological Tissues	Density ρ (kg/m ³)	Sound Speed c (m/s)
Water	1000	1480
Blood	1060	1570
Fat	920	1450
Kidney	1040	1560
Liver	1060	1570

Acoustic waves are fundamentally three dimensional, meaning variation across the (x, y, z) axes. Additionally, it has temporal dependencies since it varies on time (t) .

2.1.2. Plane waves

In [58], an acoustic wave that depends on a single spatial coordinate and time is called a plane wave. A one-dimensional wave equation fixed on z can be defined as:

$$\frac{\partial^2 p}{\partial z^2} = \frac{1}{c^2} \frac{\partial^2 p}{\partial t^2}, \quad (2.2)$$

2.2. Ultrasound imaging

2.2.1. Systems

Most medical US imaging systems employ a single transducer that works as a transceiver and is connected to the patient through a medium, such as an acoustic gel. The device emits a short duration pulse that propagates into the body encountering reflective surfaces and small scatterers as it travels. A portion of the reflected signals returns to the transducer, which then transforms it into an electrical signal that can be amplified, stored, processed, and displayed [58]. Figure 2.1 displays a block diagram of a conventional US imaging system, adapted from [59].

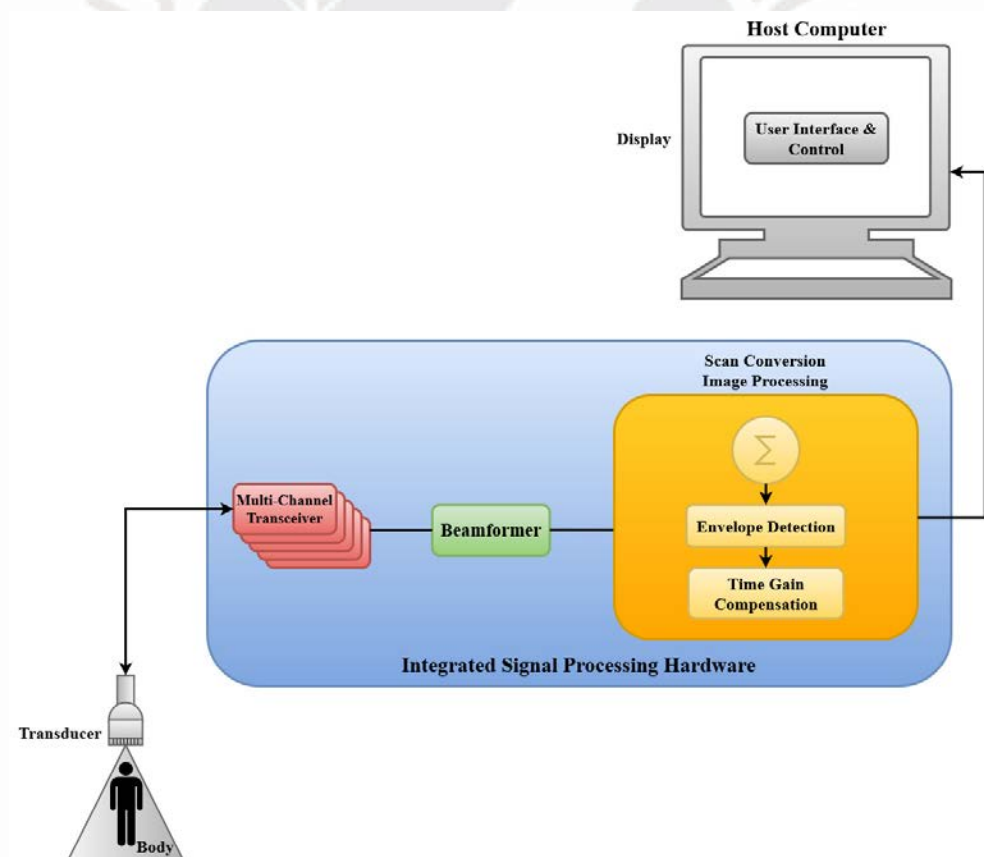


Figure 2.1: Block diagram highlighting a conventional US imaging system, adapted from [59].

2.2.2. Transducers

A transducer, whether a single or an array element, functions as a bidirectional electromechanical interface, transforming an electrical pulse into a pressure wave, to then convert it back to an electrical signal upon receiving. Although several mechanisms of conversion exist, piezoelectric is the most commonly used method in US. This type of transducer is composed of a specialized crystal.

2.2.3. Steering and focusing

Phase arrays achieve electronic beam steering and focusing with no mechanical motion from the transducer by using a compact linear array of generally 64 to 128 transducer elements, which ensure the sound stays within the image plane, while maintaining a nearly circular field pattern. A direct beam is formed during transmission by timing each element's firing to add sound coherently in the desired direction. During reception, direction sensitivity is obtained by coherently aligning and summing received signals [58].

2.3. Acoustic nonlinearity theory

In Panfilova et al. [17], the adiabatic equation was defined as Eq. (1.1), where the first coefficient A , a linear constant at a specific entropy, can be expressed as:

$$A = \rho_0 \left(\frac{\partial P}{\partial \rho} \right)_{0,s} = \rho_0 c_0^2, \quad (2.3)$$

where c_0 is the SoS. Meanwhile,

$$B = \rho_0^2 \left(\frac{\partial^2 P}{\partial \rho^2} \right)_{0,s}. \quad (2.4)$$

Making,

$$\frac{B}{A} = \frac{\rho_0}{c_0^2} \left(\frac{\partial^2 P}{\partial \rho^2} \right)_{0,s} = \frac{\rho_0}{c_0^2} \left(\frac{\partial c^2}{\partial \rho} \right)_{0,s} = 2\rho_0 c_0 \left(\frac{\partial c}{\partial P} \right)_{0,s}, \quad (2.5)$$

which is a simple measure of the amount of relative nonlinearity. Nonetheless, the coefficient of nonlinearity is far more used and is defined as:

$$\beta = 1 + \frac{1}{2}(B/A) \quad (2.6)$$

An intriguing fact of nonlinear propagation is that its effects are cumulative, leading to increasingly pronounced waveform distortion over distance, this can be seen in Figure 2.2, adapted from [59].

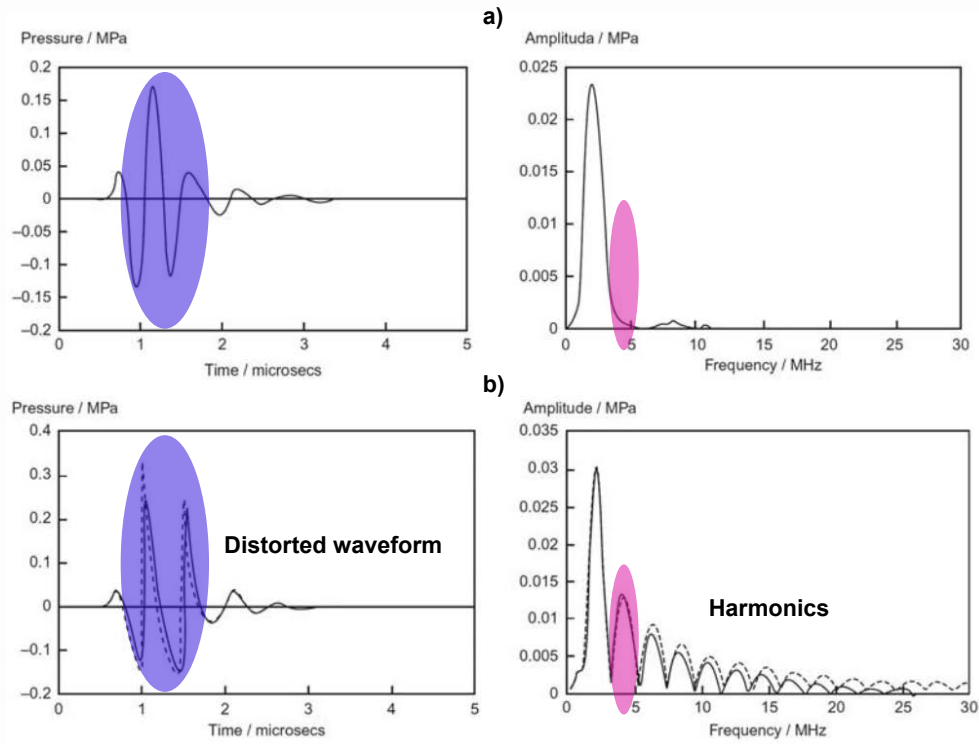


Figure 2.2: a) Linear waveform and its spectrum centered at 2.25MHz. b) Severely distorted waveform and its spectrum containing a series of harmonics centered at a multiple of the original frequency. Adapted from [59].

2.3.1. Depletion method

According to Coila et al. [55], the B/A is estimated by quantifying the reduction in the fundamental spectral component. This is accomplished using a dual-energy framework that employs two excitation pressure levels P_0 and νP_0 . The depletion term, expressed as $(\nu P_1 - P_2)$ is then derived, where P_1 and P_2 represent the envelopes of the fundamental radio frequency (RF) band at the corresponding excitation levels. Based on nonlinear acoustic theory for fluid-like media, the depletion term is proportional to the square of $(1 + B/2A)$.

First, an US transducer in pulse-echo operation registers RF backscattered signals originating at depth z with amplitude pressures $P'_{ni}(z)$ corresponding to the n -th band, and i -th excitation. At the lowest pressure level P_0 , $i = 1$,

$$P'_{11}(z) = \frac{\gamma(z)}{z} P_{11}(z) e^{-\alpha_1 z}, \quad (2.7)$$

here P'_{11} (P'_{ni}) denotes the incident pressure at z . The measured pressure can be expressed as the fundamental band pressure at z , with a known attenuation coefficient α_1 from the transducer to z , and with the reflectivity term $\gamma(z)$. Similarly, at νP_0 , $i = 2$.

$$P'_{12}(z) = \frac{\gamma(z)}{z} P_{12}(z) e^{-\alpha_1 z}. \quad (2.8)$$

Then, since the model was based on the weak nonlinearity theory of attenuation in fluid-like media, the propagated pressure can be denoted as:

$$P_{11} \approx P_0 e^{-\alpha_1 z} - P_0 e^{-\alpha_1 z} \frac{1}{32} \Gamma_0^2 [1 - e^{-2\alpha_1 z}]^2, \quad (2.9)$$

where Γ_0 is the Gol'dberg number, a metric quantified based on the medium's acoustic parameters, defined as

$$\Gamma = \frac{2\pi f_0 \beta P_0}{\rho_0 c_0^3 \alpha}, \quad (2.10)$$

In the case of the high excitation level, $i = 2$,

$$P_{12} \approx \nu P_0 e^{-\alpha_1 z} - \nu P_0 e^{-\alpha_1 z} \frac{1}{32} \nu^2 \Gamma_0^2 [1 - e^{-2\alpha_1 z}]^2. \quad (2.11)$$

Subsequently, following $(\nu P_1 - P_2)$, the depletion term can be expressed as:

$$\nu P_{11} - P_{12} \approx [\nu^3 - \nu] P_0 e^{-\alpha_1 z} \frac{1}{32} \Gamma_0^2 [1 - e^{-2\alpha_1 z}]^2. \quad (2.12)$$

Afterward, substituting Eq. (2.7) and (2.8) into (2.12), gives a valid approximation when $\Gamma_0 < 1$,

$$\nu P'_{11} - P'_{12} = [\nu^3 - \nu] P_0 \frac{1}{32} \Gamma_0^2 [1 - e^{-2\alpha_1 z}]^2 \frac{\gamma}{z} e^{-2\alpha_1 z}. \quad (2.13)$$

Thereafter, employing data from a reference phantom acquired under the same settings and dividing by Eq. (2.13), it results

$$\beta = \beta_R \cdot \sqrt{\frac{[\nu P'_{11} - P'_{12}][P'_{11,R}]}{[\nu P'_{11,R} - P'_{12,R}][P'_{11}]}} \frac{(1 - e^{-2\alpha_{1,R} z})}{(1 - e^{-2\alpha_1 z})} \frac{\alpha_1}{\alpha_{1,R}}. \quad (2.14)$$

Finally, from Eq. (2.6) and (2.14), the B/A can be estimated.

2.3.2. Inversion approach

In Coila et al. [55], the B/A estimates were assumed to be cumulative values (B/A_C) encapsulating data of local B/A values up to a specific depth, relating them to the average of the local values denoted as (B/A_L). For instance, at the H -th pixel along the axial direction, a valid approximation is

$$\frac{B}{A_{H,C}} = \frac{1}{H} \sum_{h=1}^H \frac{B}{A_{h,L}}. \quad (2.15)$$

By the following map, the B/A_L values were obtained

$$\begin{bmatrix} \frac{1}{q+1} & 0 & \cdots & 0 \\ \frac{1}{q+2} & \frac{1}{q+2} & \cdots & 0 \\ \vdots & \vdots & \ddots & \vdots \\ \frac{1}{H} & \frac{1}{H} & \cdots & \frac{1}{H} \end{bmatrix} \times \begin{bmatrix} \frac{B}{A_{q+1,L}} \\ \frac{B}{A_{q+2,L}} \\ \vdots \\ \frac{B}{A_{H,L}} \end{bmatrix} = \begin{bmatrix} \frac{B}{A_{q+1,C}} - \frac{q}{q+1} \frac{B}{A_{q,C}} \\ \frac{B}{A_{q+2,C}} - \frac{q}{q+2} \frac{B}{A_{q,C}} \\ \vdots \\ \frac{B}{A_{H,C}} - \frac{q}{H} \frac{B}{A_{q,C}} \end{bmatrix} \quad (2.16)$$

where the initial cumulative values q were unavailable, if X and Y matrices were considered as local and cumulative B/A maps, respectively, consisting of m rows and n columns, where $m = H - q$, Eq. (2.16) can be applied to every B/A map column through a mapping with a triangular matrix M .

By assembling the n equations using the Kronecker product of M and I_n matrices, every element of X and Y can be mapped at the same time.

2.4. Datasets

2.4.1. k-Wave toolbox

A MATLAB toolbox designed for an efficient and straightforward simulation and reconstruction of photoacoustic wave fields. The toolbox provides functions that can be categorized into four main groups: photoacoustics or ultrasonic wave fields simulations, photoacoustics image reconstruction, creation of geometric shapes, and utility and system functions [60].

2.4.2. Experiment description

For instance in [55], the Depletion Method was tested using the k-Wave toolbox. For both numerical phantoms (sample and reference), RF data was generated using a linear array transceiver of 128 elements with a 5 MHz center frequency pulse. For low and high excitation levels 80 kPa and 400 kPa were used. A scattering media was simulated with a mean of $\mu = 1000$ (kg/m^3) and a standard deviation of $\sigma = 2\%$, and an ACS = 0.5 dB/cm/MHz. Lastly, while creating the B/A sample map, the background and circular inclusion were assigned B/A values of 6 and 11, respectively; in contrast to the homogeneous B/A reference map. Figure 2.3 display the B-mode visualization alongside the ground truth B/A sample map, adapted from [55].

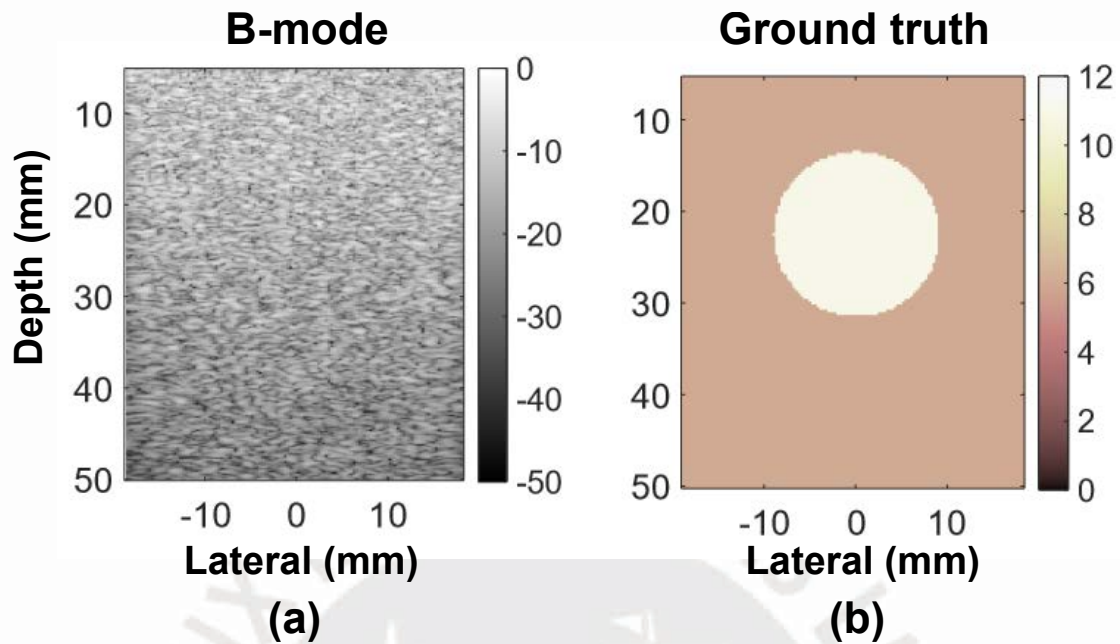


Figure 2.3: (a) B-mode display (no visible contrast of the inclusion). (b) Ground truth B/A map with the values assigned to the background and the inclusion. Adapted from [55].

2.5. B/A maps reconstruction

2.5.1. Filtering

The data from both the sample and reference were filtered before the acquisition of the envelopes. For instance, the Finite Impulse Response filter (FIR), characterized by its finite duration impulse response indicating they reach zero after a finite number of sample points, was used. Figure 2.4 illustrates the FIR filter with its corresponding settings and Fig. 2.5 exhibits the clear comparison between the original and filtered data.

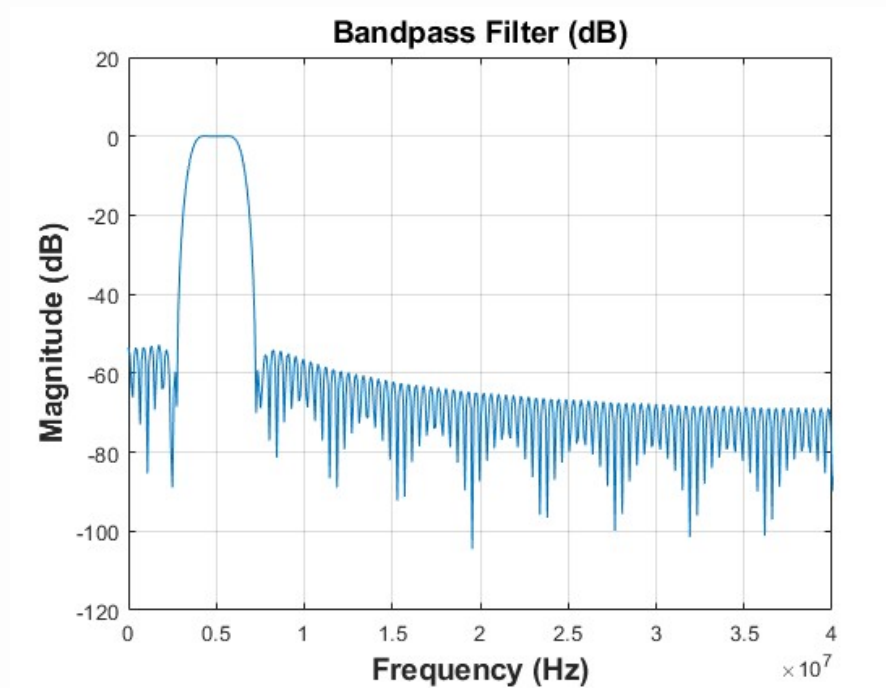


Figure 2.4: Band-pass filter [3.5-6.5] MHz at $f_0 = 5$ MHz and an order of 200.

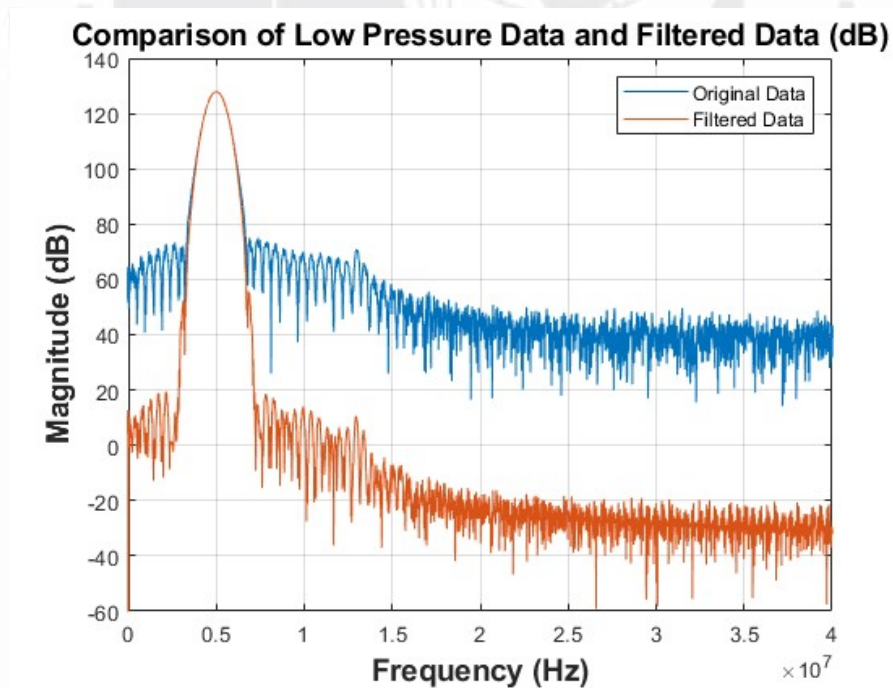


Figure 2.5: Comparison between the low-pressure (80 kPa) original and filtered data at $f_0 = 5$ MHz.

2.5.2. Implementation

For every n -th band, i -th excitation, P'_{ni} was estimated by averaging the envelopes of 4 filtered RF-lines by using an overlap of 2. Simultaneously, $P'_{ni,R}$ was obtained by averaging the envelopes of 128 filtered RF-lines.

Then, a moving mean filter with a window of 10 wavelengths was implemented for P'_{ni} and $P'_{ni,R}$ to smooth the data by reducing noise and fluctuations before operating with them in Eq. (2.14) of the depletion method, after which the inversion approach was applied obtaining a mean percentage error (MPE) of 7.9% . Figure 2.6 exhibits the depletion image and its inversion, as described in the experiment description section.

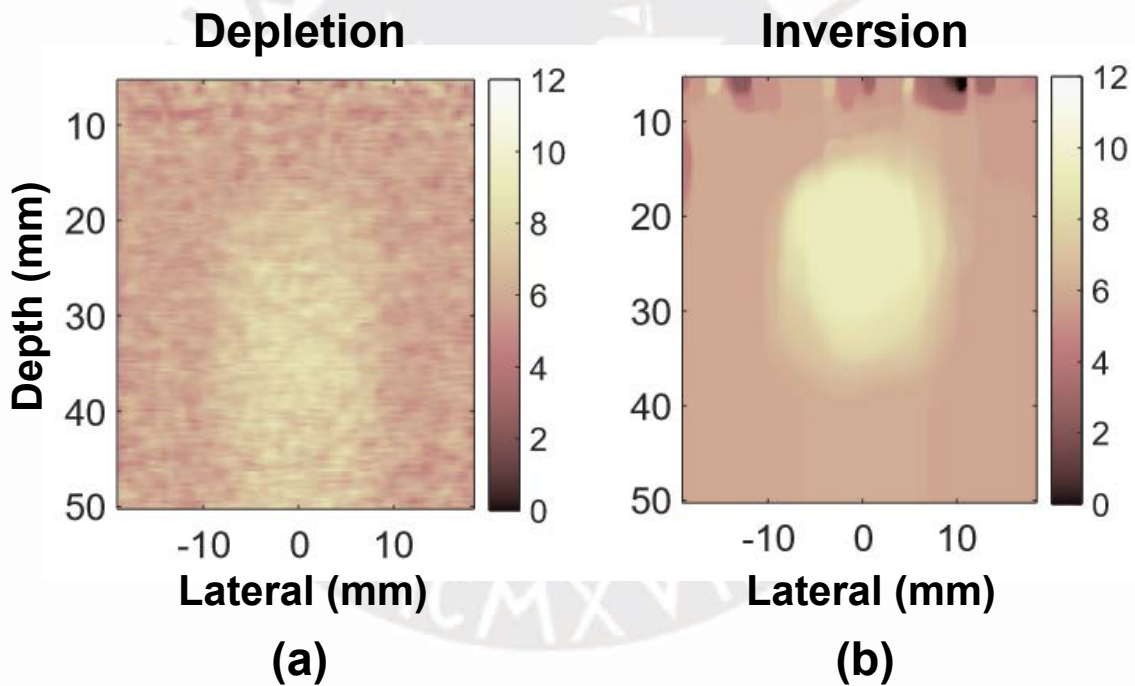


Figure 2.6: (a) Depletion method image. (b) Inversion approach of (a). Adapted from [55].

2.6. Full angular spatial compounding

As previously noted, FASC improves image quality by acquiring images from multiple views and combining them to produce a more enhanced final image. A technique developed to reduce speckle and enhance contrast in B-mode displays. This can be achieved by sampling the same ROI at different positions, allowing the receiving envelopes to be averaged reducing the deviation of the derived image [48, 61].

As stated by Lavarello et al. [62], the precision of average scatterer diameter (ASD) estimates was enhanced through multiple-viewing data, as evidenced by a decrease in variability. For instance, it was experimentally validated when using ROIs of size 10λ by 10λ and 32 viewing angles, the ASD standard deviation decreased from 24.6 to 4.8 μm .

In [49], FASC images were generated by associating the median value of 30 different viewing angles to each pixel. This approach resulted in less variance compared to single view estimates. The variance reductions were close to 90% for Phantom 1 and over 90% for Phantom #2 in both inclusion and background. Figure 2.7 contrasts the attenuation images between single view and FASC, adapted from [49].

In the current work, the FASC technique will be applied after the inversion of the depletion method for each position of the transducer, allowing an improved visualization and localization of the ROI. Figure 2.8 shows the technique schematically, adapted from [63].

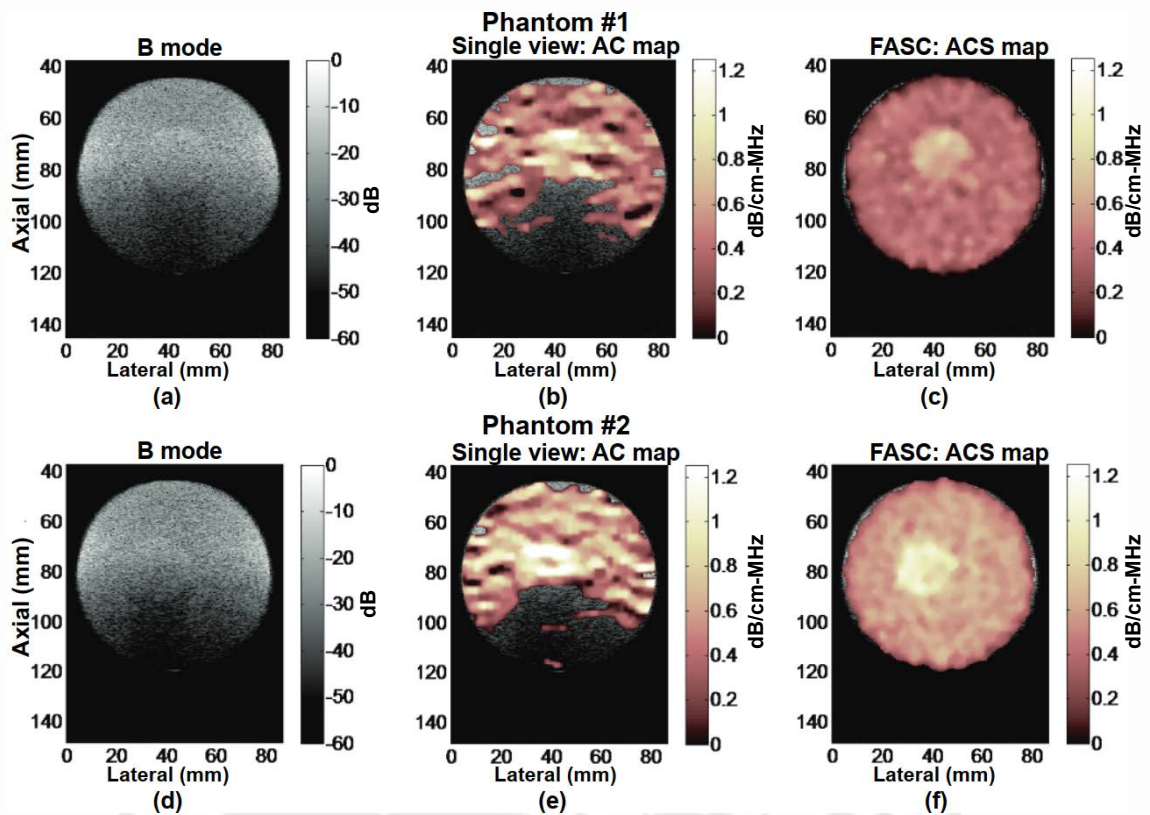


Figure 2.7: [On both phantoms] (a), (d): Single view B-mode output. (b), (e): Single view attenuation coefficient displays. (c), (f): FASC attenuation maps, adapted from [49].

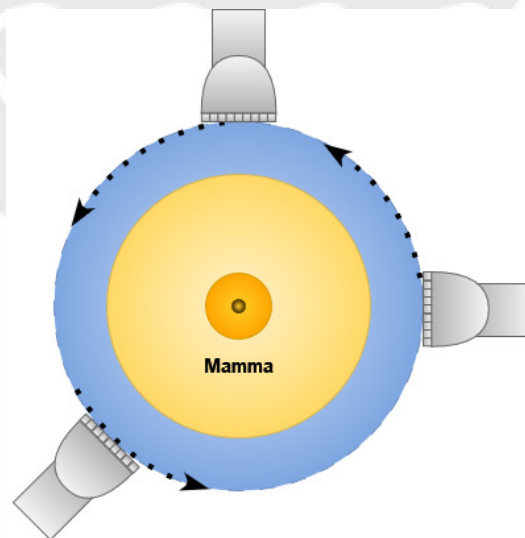


Figure 2.8: FASC illustration: US transducer rotating around the breast during data acquisition, adapted from [63].

2.7. Evaluation metrics

To evaluate the performance of the implemented methods, metrics such as the mean, standard deviation, CNR and NRMSE of the estimated B/A maps values will be calculated.

- Statistical metrics: Such as mean (\bar{x}) and standard deviation (σ).
- Contrast to noise ratio (CNR) to evaluate the quality of the B/A maps.

$$\text{CNR} = \frac{|\bar{x}_{inc} - \bar{x}_{back}|}{\sqrt{\sigma_{inc}^2 + \sigma_{back}^2}}, \quad (2.17)$$

- Normalized Root Mean Square Error (NRMSE) to quantify the error between estimated values and ground truth (or reference) values, normalized by the reference.

$$\text{NRMSE} = \sqrt{\frac{1}{Q} \sum_i^Q \left(\frac{\beta_i^e - \beta_i^o}{\beta_i^o} \right)^2} \cdot 100\%, \quad (2.18)$$

where β^e and β^o represent the estimated and ground truth B/A maps values, respectively.

Q denotes the amount of pixels in the ROI for metrics.

Chapter III

Simulation framework and B/A estimation pipeline using depletion and FASC techniques

This chapter offers a detailed account of the methodology developed to improve breast ultrasound imaging by integrating the depletion method with FASC.

3.1. Procedure sequence

The procedure begins with the acquisition of raw ultrasound data, then processed by a beamformer to generate RF data which are analyzed using the depletion method to estimate B/A_C values, subsequently converted into B/A_L estimates through an inversion approach. This process is repeated across all angular views. Figure 3.1 provides a clear overview of the steps involved in the procedure.

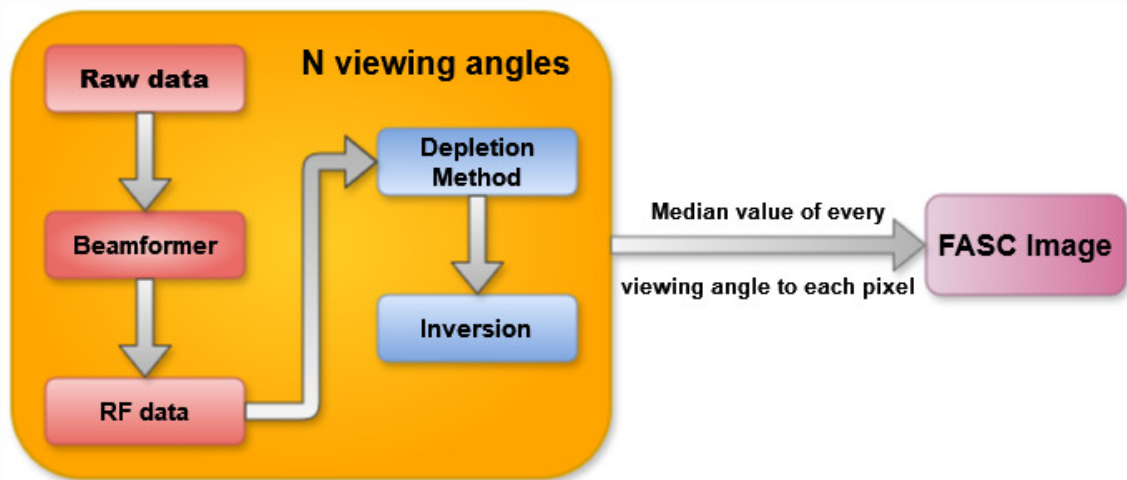


Figure 3.1: Block diagram of the procedure sequence.

3.2. Proposed model

For the proposed configuration of the breast tissue model, a phantom with embedded inclusions is gradually laterally shifted across a horizontal plane at a chosen rotation angle, θ , within a water interface. Meanwhile, a linear array transducer remains stationary, capturing data as the phantom rotates to provide a 360-degree view. This setup is designed to achieve a view of the phantom from every angle, enhancing the accuracy of the imaging process.

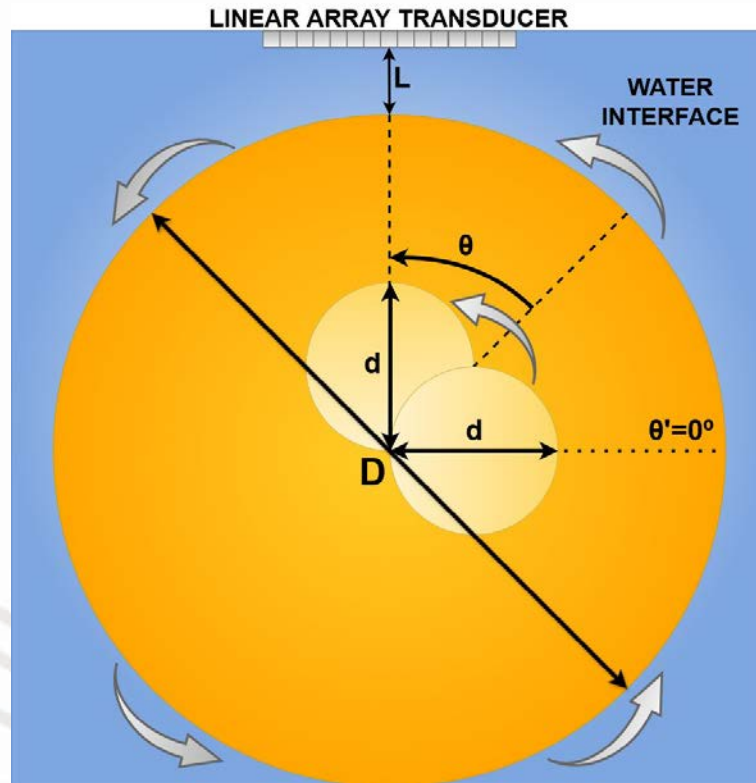


Figure 3.2: Proposed model configuration for breast tissue: A phantom, along with its inclusion being laterally displaced a specified rotational angle θ . Initial reference angle for the rotation ($\theta' = 0^\circ$). L: transducer-phantom distance. D: phantom diameter. d: inclusion diameter.

3.3. Simulation setup

3.3.1. Water interface

It plays a crucial role in ultrasound simulations and experiments, acting as the medium for ultrasound wave propagation between the transducer and the phantom. In breast tissue simulations, water is commonly used due to its low acoustic attenuation, which minimizes signal loss and allows for clear visualization of wave propagation [63]. Table 3.1 overviews the acoustic characteristics of water.

Table 3.1: Acoustic properties of water used as an interface in ultrasound simulations

Density ρ (kg/m ³)	Attenuation Coefficient (dB/cm/MHz ²)	Reference	Acoustic Nonlinearity Parameter (B/A)
1000	0.0022	[12]	5.1

3.3.2. Numerical phantom design

Created to replicate the acoustic properties of breast tissue, the phantom is designed as a circular structure with dimensions carefully selected to simulate a realistic tissue environment. The numerical phantom's diameter, ranging from 4 to 6 cm, was derived from anthropometric data. Table 3.2 presents the Inframammary Fold-to-Nipple Distance (IR) and the corresponding calculated ratio (R) in different countries, adapted from [64]. Figure 3.3 exhibits IR and R, adapted from [65].

Table 3.2: Comparison of IR and R between countries

Country	IR (cm)	R (cm)	Reference
Vietnam	6.8	4.3	[64]
Arabia	7.7	4.9	[66]
Turkey	8.3, [7.3R - 7.4L]	5.2, [4.6R - 4.7L]	[67], [65]
Italy	9.26	5.8	[68]

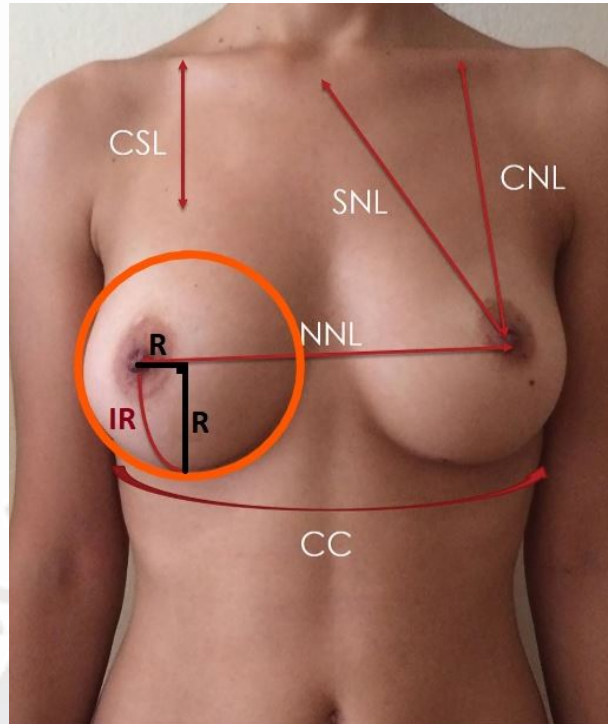


Figure 3.3: Breast anthropometric measurements diagram, adapted from [69].

Inclusions are incorporated within the phantom to represent abnormalities commonly found in breast tissue. These inclusions can vary in size, shape, and acoustic properties, such as density, B/A parameter, and attenuation. Table 3.3 shows the acoustic properties of the phantoms used in simulation.

Table 3.3: Acoustic properties of the numerical phantoms and their inclusions used in simulations

Phantom	Emulates	Density (kg/m³)	Attenuation Coefficient (dB/cm/MHz)	Acoustic Nonlinearity Parameter
Inclusion M	Multiple Myeloma of the Breast	1070 ± 20	0.25	5.5
Inclusion N	Adenocarcinoma Metastatic in Breast	1050 ± 20	0.28	6.5
Inclusion P	Lymphnode in Breast	1040 ± 20	0.33	8
Background	Breast	1020 ± 20	0.4	10

3.3.3. Transducer specifications

The transducer used in this study is modeled as a 2D linear array and is positioned at a distance of 1 to 1.5 cm from the phantom. Table 3.4 presents the transducer configuration.

Table 3.4: Transducer configuration specifications used in simulations

Number of elements	Pitch (mm)	Central Frequency (MHz)
128	0.48	4

3.3.4. k-Wave toolbox

The MATLAB toolbox permits the creation of customized phantoms and precise specification of their acoustic properties, such as SoS, density, and attenuation coefficients [60]. Table 3.5 provides an overview of the computer hardware and software configurations used to perform the simulations.

Table 3.5: Hardware and software specifications for simulation environment

Processor	Memory	Graphics Card
Intel Core i9-12900, 3.2 GHz	64 GB	NVIDIA GeForce RTX 3070 Ti, 8 GB VRAM

3.4. Dataset construction

Table 3.6: Key characteristics for the dataset construction

Version Name	Number of Inclusions	Shape of Inclusion	Size of Inclusion (cm)	Type of Inclusion	Transducer-Phantom (cm)
V1star		star-cross	1		
V1a			1		
V1a1	1	circle	0.875	M	0
V1a2			0.750		
V1a3			0.625		
V1a4			0.500		
V1b			1		
V2a	2	circle	0.750	M & N	0
V2b					1
V3a	3	circle	0.750	M, N & P	0
V3b					1

3.5. RF data acquisition

3.5.1. RF signal generation

RF signals are generated using a linear array transducer configured as previously described. To simulate both low and high-energy conditions, a dual-energy approach is employed, using two distinct excitation pressure levels 80 and 400 kPa, which allows for the comparison of signal behavior under different acoustic pressures. The transducer's elements emit the signals simultaneously. This approach is crucial for capturing variations in the fundamental frequency band of the backscattered RF data.

3.5.2. RF data collection process

RF data is acquired at each excitation pressure level throughout the entire phantom. While the transducer remains stationary, the phantom is systematically rotated within a water interface to capture a full 360° view. This approach improves data quality by offering multiple perspectives of the region of interest. The collected RF lines for each pressure level are then stored and utilized for B/A estimation using the depletion method.

3.6. RF data process

3.6.1. Depletion method implementation

To achieve precise B/A estimation, a processing step on the RF data was implemented by focusing exclusively on a defined area of interest in numerical phantoms. By restricting the analysis to a specific depth, data portions that don't meaningfully contribute to the results and could introduce noise or unwanted artifacts are excluded. Thereby, narrowing down the dataset to the start and end of the lateral edge of the numerical phantom, as shown in Figure 3.4. Hence

reducing interference from less relevant sections, which can often distort or complicate the analysis. As detailed in Table 3.6, this selective focus is applied in both scenarios: when the transducer is placed approximately 1 cm from the phantom, and when it is directly adjacent to it without any significant gap.

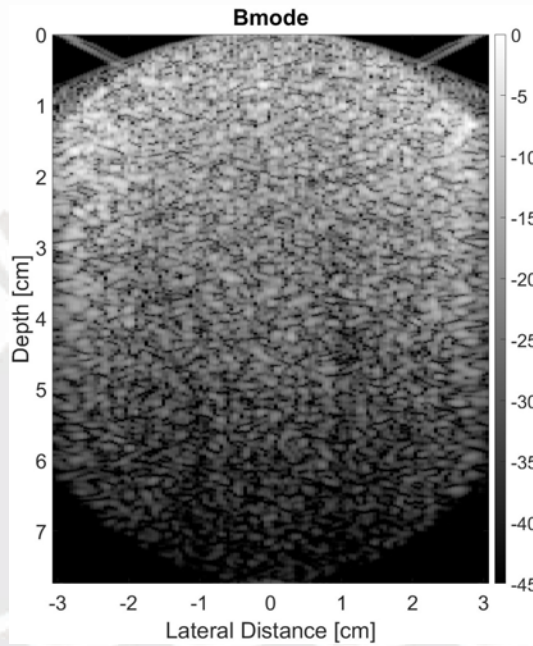


Figure 3.4: [B-mode image]: Sample low-pressure (80 kPa) $\theta = 90^\circ$.

Then a bandpass filter is applied to isolate the fundamental frequency component, thereby minimizing noise and enhancing signal clarity. The filter was designed with a center frequency of 4 MHz with lower and upper bounds of 2.5 and 5.5 MHz cutoff frequencies, respectively. To ensure optimal processing of the RF data in the time domain, a 200 order filter is selected. The filter implemented is the *fir1* function from MATLAB. FIR (Finite Impulse Filters) filters work ideally for isolating specific frequency ranges without altering the signal's shape over time. Fig. 3.5 compares the pre and post-filtered data.

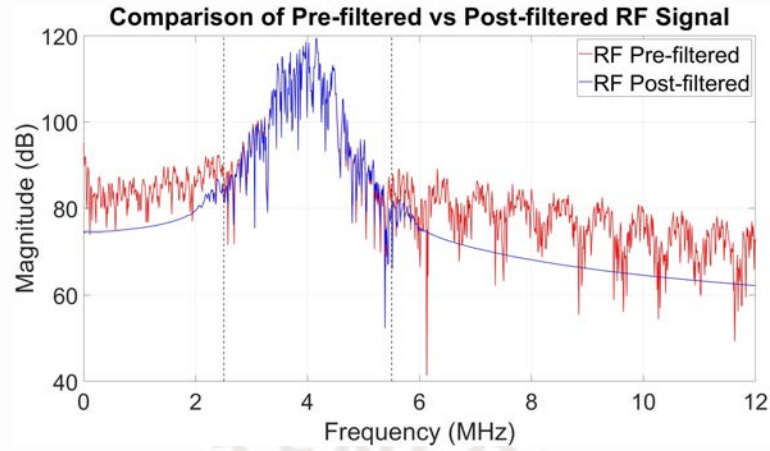


Figure 3.5: Comparison between the sample low-pressure (80 kPa) Pre-filtered and Post-filtered middle RF signal in the frequency domain, $\theta = 90^\circ$.

Once the filtering is complete, detailed attenuation and B/A maps reveal the essential acoustic features of both the sample and reference, are created. Starting with the attenuation map, coefficients are calculated to indicate how much the ultrasound signal diminishes as it moves through different regions of the sample. These coefficients, taken from the RF data at various depths, allow us to build a map that visualizes signal loss throughout the sample, bringing out areas with unique acoustic properties.

With the attenuation coefficients established, the process continues with generating the B/A map to capture the sample's nonlinearity under varying pressures. This step involves calculating a parameter called gap, which represents the difference between signal envelopes at low (80 kPa) and high (400 kPa) pressures. It reflects how much the sample's response deviates from linearity and serves as the foundation for estimating B/A values.

Combining gap and attenuation values produces a B/A map that illustrates nonlinearity across the sample at different depths and positions. These frequency-isolated maps provide insight into the sample's internal structure and acoustic properties, allowing for thorough analysis of attenuation and nonlinearity while preserving signal clarity.

3.6.2. Inversion approach

Eq. (3.1), presents a simplified version of Eq. (2.16)

$$A \times u = b \quad (3.1)$$

where A is the matrix that captures the relationship among the local B/A values and the cumulative estimates, x represents the unknown parameters we are trying to determine, and b corresponds to the observed cumulative B/A values. To solve it an inverse problem is formulated as a minimization task, shown in Eq.(3.2)

$$\arg \min_u \frac{1}{2} \|b - Au\|_2^2 + \mu \mathcal{R}(u), \quad (3.2)$$

in which $\frac{1}{2} \|b - Au\|_2^2$ represents the fidelity term, which is based on the ℓ_2 -norm and measures how well the model Ax fits the data b , μ is the regularization parameter, that balances the trade-off amid the fidelity term and the regularization term, $\mathcal{R}(u)$, which can enforce smoothness, sparsity, or any other desired property, such as Total Variation.

$$\mathcal{R}(u) = TV(u) = \sqrt{(\nabla_x u)^2 + (\nabla_z u)^2}. \quad (3.3)$$

The gradients $\nabla_x u$ and $\nabla_z u$ are the partial derivatives of u in the distinct directions, respectively [69].

The current algorithm uses two regularization parameters, μ and τ , to balance data fidelity and smoothness. μ determines how closely the solution (the estimated B/A map) aligns with the measured data. Higher values prioritize accuracy, which can let in more noise, while lower values provide smoother results but may sacrifice some accuracy. τ adjusts the (TV) regularization, which helps to keep the solution smooth. Higher values produce a cleaner, smoother result

with less noise, but might lose some fine details. Lower values preserve more of the original details but may let through a bit more noise.

3.6.3. Full angular spatial compounding

A 10-degree separation acquisition between viewing angles in FASC was chosen to balance the computational time and image quality improvement. While using a smaller rotational angle, such as 1 degree, could provide more data points, reduce noise, and increase the accuracy of the compounded image, it would also significantly raise the number of scans needed. Thereby, leading to longer processing times and greater use of computational resources. By selecting a 10-degree interval, we can capture enough angular views (36 in total for a complete 360-degree rotation) to improve image quality while keeping both time and computational demands manageable.

Each simulation, representing a single position, takes roughly 10 minutes, bringing the total computation time to about 12 hours for all the simulations. The assessment will focus on the number of viewing angles, equivalent to the angular separation between them.

As shown in Figure 3.1, the FASC image is created by taking the median value of each pixel across all views. The median is preferred over the mean because it is more resilient to outliers and noise. It selects the central value from all viewing angles, effectively filtering out extreme variations and offering a more stable and reliable estimate of the true signal. Meanwhile, when the mean is used, these outliers can distort the result, causing inaccuracies in the FASC image. Hence, the use of the median ensures that the quality of the final image is not as susceptible to random noise or occasional anomalies, making it a more suitable option for FASC.

Chapter IV

Quantitative evaluation of *B/A* imaging: Impact fo FASC and TV regularization

This chapter presents a quantitative and qualitative evaluation of the proposed *B/A* imaging method, focusing on the effect of FASC and TV regularization. Several simulated phantoms are examined to evaluate the effects of two key parameters: the number of viewing angles and the regularization parameter μ . Performance is quantified using descriptive statistics, CNR, MPE and NRMSE within defined regions of interest.

4.1. Computer simulation recap

Each dataset version features distinct configurations, altering the number, shape and type of inclusions, as well as the transducer-phantom distance, to evaluate the method under diverse conditions.

4.1.1. Dataset versions: V1star

This dataset version introduces a single star-cross inclusion ($d = 2$ cm) embedded within a homogeneous circular background ($D = 8$ cm), surrounded by a water interface. The star-shaped geometry breaks the symmetry of isotropic structures and generates geometric anisotropy because the inclusion does not present the same profile in all directions. The inclusion M emulates the acoustic characteristics of Multiple Myeloma, while the circular background represents healthy breast tissue, and the surrounding region corresponds to water, as specified in Tables 3.1 and 3.3. The transducer is adjacent to the phantom ($L = 0$ cm). Figure 4.1 illustrates the B/A , attenuation, and density maps corresponding to this configuration.

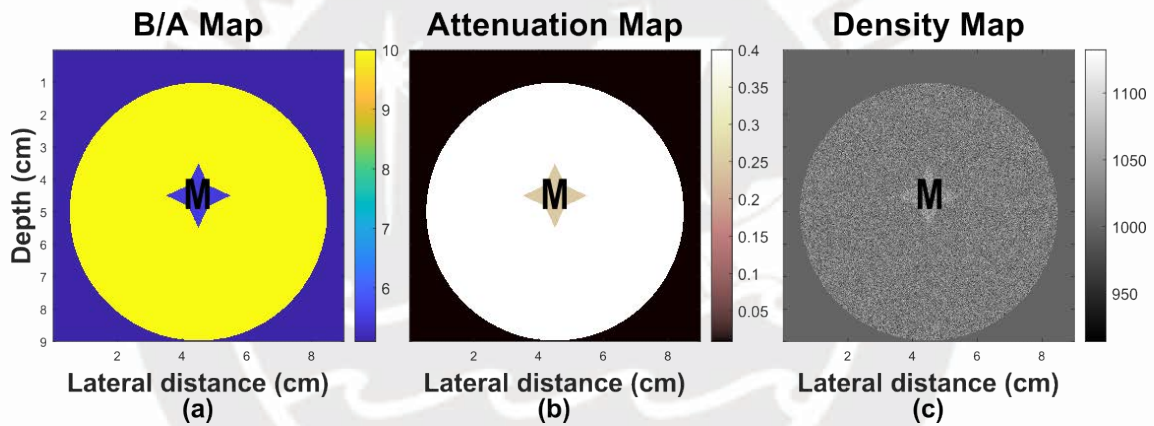


Figure 4.1: [Dataset V1star, $\theta = 90^\circ$] (a) B/A map, (b) Attenuation Coeff. map, (c) Density map

4.1.2. Dataset versions: V1a & V1b

This dataset versions present a single circular inclusion ($d = 2$ cm) embedded within a homogeneous circular background ($D = 8$ cm) and surrounded by a water interface. The circular geometry provides an isotropic configuration, as the inclusion exhibits the same profile in all directions, in contrast to irregular or anisotropic shapes. The inclusion M emulates the acoustic characteristics of Multiple Myeloma, while the circular background represents healthy breast tissue, and the surrounding region corresponds to water, as specified in Tables 3.1 and 3.3.

Two configurations were defined to evaluate the influence of transducer-phantom proximity on imaging performance:

1. V1a: The transducer is in contact with the phantom ($L = 0$ cm).
2. V1b: The transducer is positioned with a separation of ($L = 1$ cm) from the phantom.

Furthermore, in the case of V1a, additional sub-versions were created by progressively reducing the diameter of the inclusion, as seen in Table 3.6. It allows a systematic analysis of inclusion size effects on the reconstructed maps. Figure 4.2 illustrates the B/A , attenuation, and density maps corresponding to the main 2 configurations.

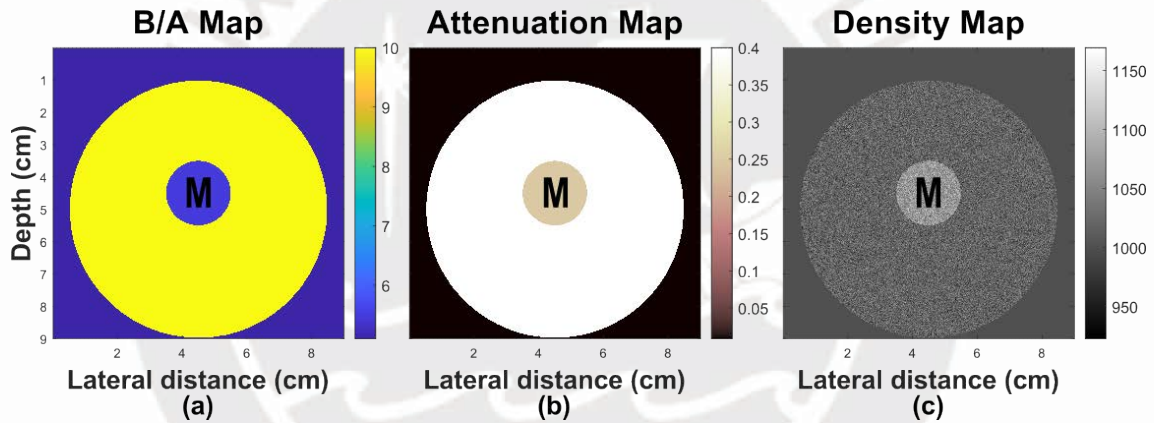


Figure 4.2: [Dataset V1a-b, $\theta = 90^\circ$] (a) B/A map, (b) Attenuation Coeff. map, (c) Density map

4.1.3. Dataset versions: V2a & V2b

This dataset versions introduce two circular inclusions ($d = 1.5$ cm) embedded within a homogeneous circular background ($D = 8$ cm) and surrounded by a water interface. Both inclusions provide an isotropic configuration. The first inclusion, denoted as M, emulates the acoustic characteristics of Multiple Myeloma, while the second inclusion N, corresponds to Adenocarcinoma Metastatic. The circular background represents healthy breast tissue, and the surrounding region corresponds to water, as specified in Tables 3.1 and 3.3. The purpose is to

evaluate performance in scenarios involving multiple inclusions with distinct acoustic properties. Two configurations were defined to evaluate the influence of transducer-phantom proximity on imaging performance:

1. V2a: The transducer is in contact with the phantom ($L = 0$ cm).
2. V2b: The transducer is positioned with a separation of ($L = 1$ cm) from the phantom.

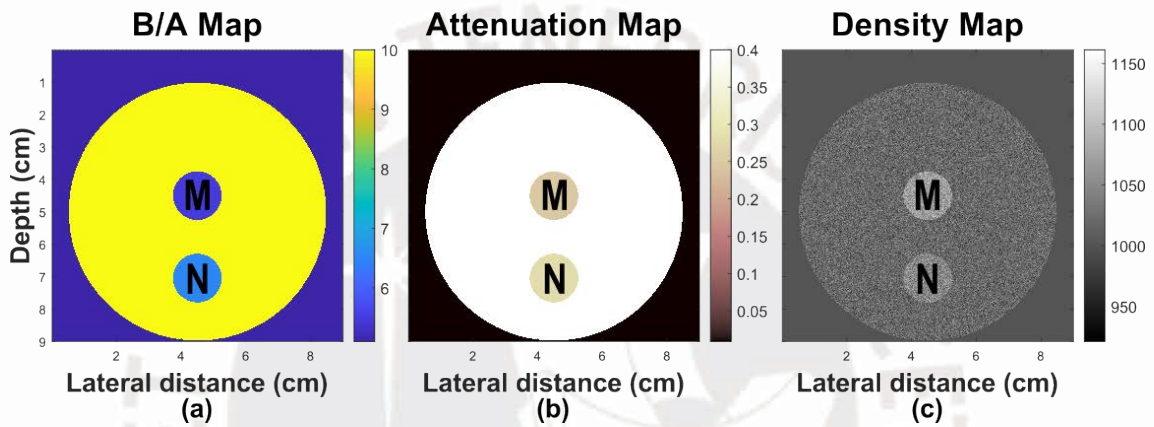


Figure 4.3: [Dataset V2a-b, $\theta = 90^\circ$] (a) B/A map, (b) Attenuation Coeff. map, (c) Density map

4.1.4. Dataset versions: V3a & V3b

This dataset versions present three circular inclusions ($d = 1.5$ cm) embedded within a homogeneous circular background ($D = 8$ cm) and surrounded by a water interface. As in the previous cases, the circular geometry provides an isotropic configuration. The inclusions correspond to different pathological breast tissue conditions. Inclusion M, N and P emulate the acoustic characteristics of Multiple Myeloma, Adenocarcinoma Metastatic, and Lymph node, respectively. The circular background represents healthy breast tissue, and the surrounding region corresponds to water, as specified in Tables 3.1 and 3.3. The purpose is to evaluate performance in scenarios involving multiple inclusions, including one (P) whose acoustic characteristics are relatively closed to those of the background. This configuration tests the robustness

of the method in detecting inclusions with low contrast. Two configurations were defined to evaluate the influence of transducer-phantom proximity on imaging performance:

1. V3a: The transducer is in contact with the phantom ($L = 0$ cm).
2. V3b: The transducer is positioned with a separation of ($L = 1$ cm) from the phantom.

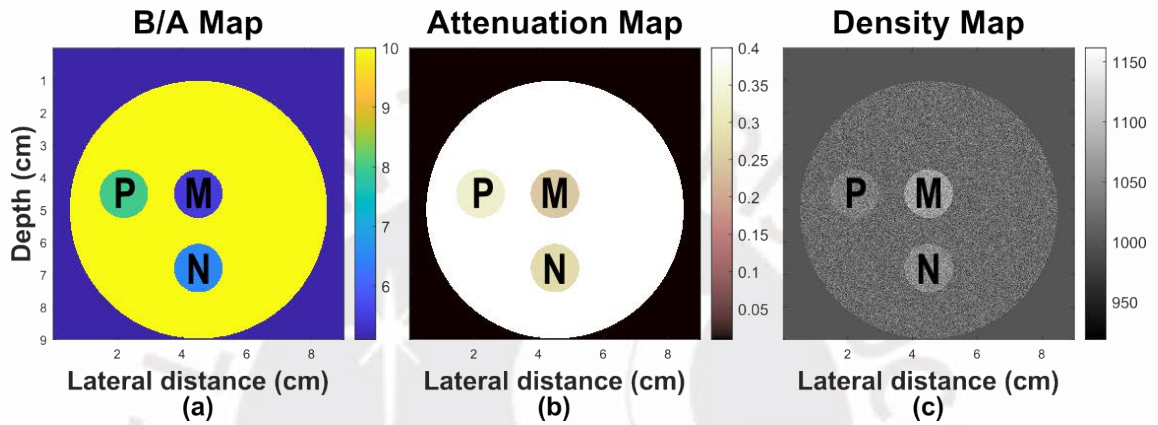


Figure 4.4: [Dataset V3a-b, $\theta = 90^\circ$] (a) B/A map, (b) Attenuation Coeff. map, (c) Density map

4.2. Impact of the number of viewing angles on reconstruction performance

This section analyzes the influence of FASC on US imaging performance across different dataset configurations.

4.2.1. Dataset versions: V1star

For the star-cross inclusion in Dataset V1star, the progressive integration of multiple viewing angles in the FASC reconstructions (Fig. 4.5) reveals a clear enhancement in image quality and spatial coherence. As the number of views increases from one to 4, 12, and 36, the reconstructed B/A maps exhibit decreased variability, yielding a more homogeneous background and clearer-defined inclusion edges.

Even though the B/A values remain overestimated compared to the ground truth (dashed lines), the reconstructions demonstrate enhanced spatial uniformity and reduced speckle variability, as illustrated in Fig. 4.6.

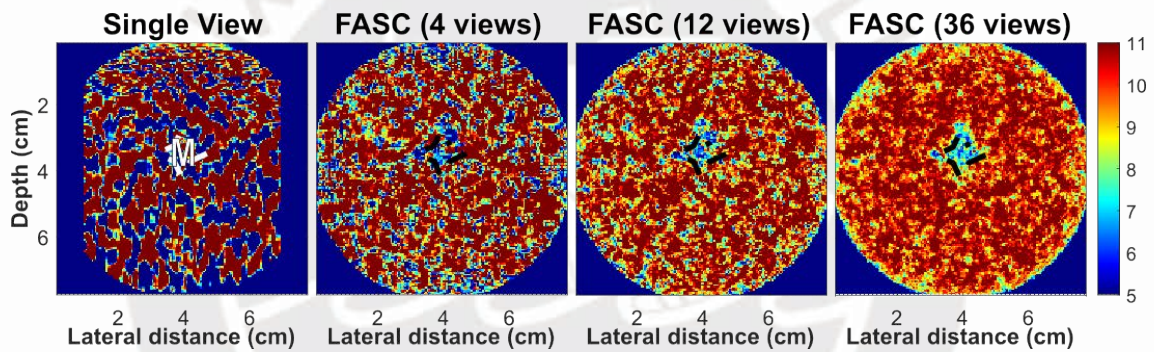


Figure 4.5: [Dataset V1star, $\theta = 90^\circ$] B/A maps of a star-cross shaped inclusion. Results are shown for both single view and FASC reconstructions with 4, 12 and 36 views. The transducer is adjacent to the phantom.

The quantitative analysis supports these observations: the mean and standard deviation trends (Fig. 4.6) demonstrate that the estimated B/A values stabilize and the variability within both the background and the inclusion region decrease as the number of views increases. Likewise, the CNR and NRMSE (Fig. 4.7) show consistent improvement with the addition of multiple viewing angles, confirming the advantage of FASC.

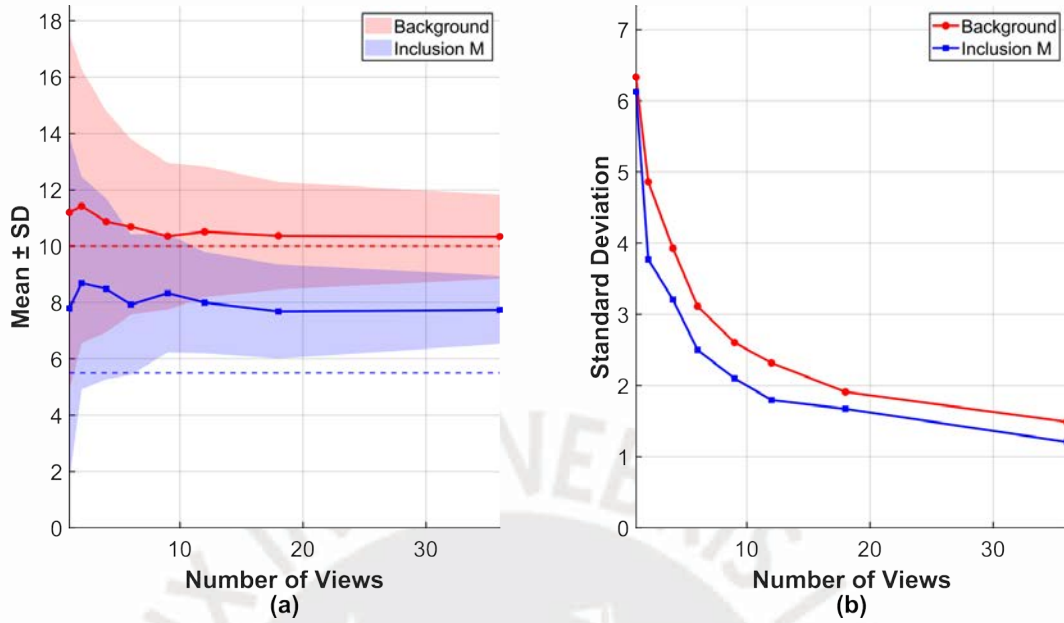


Figure 4.6: [Dataset V1star]: (a) Mean \pm SD. The horizontal dashed lines represent the ground truth values for the background (red), and inclusion M (blue). (b) Standard Deviation.

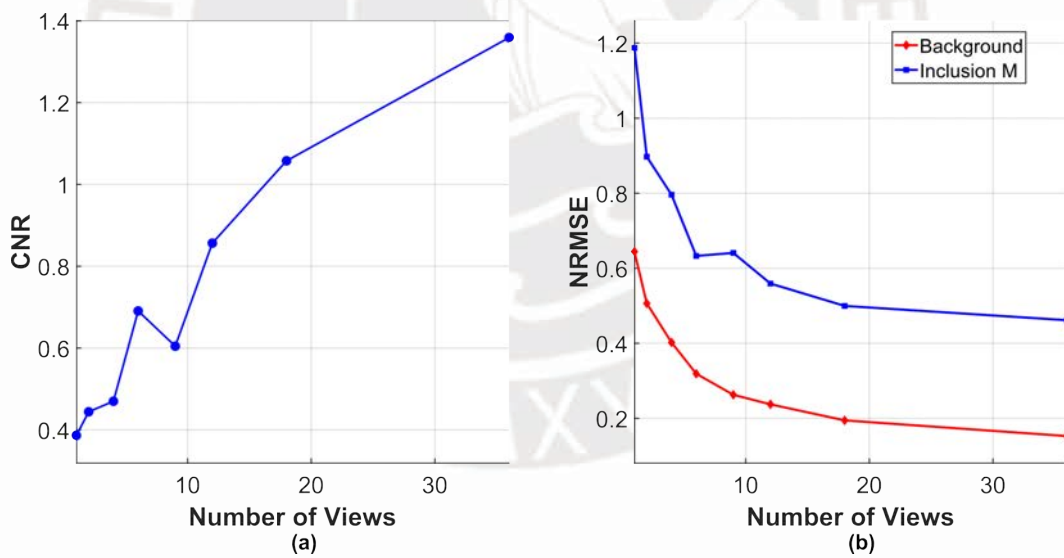


Figure 4.7: [Dataset V1star]: (a) CNR. (b) NRMSE.

4.2.2. Dataset versions: V1a & V1b

For the single circular inclusion in V1a, the progressive integration of multiple viewing angles in the FASC reconstructions (Fig. 4.8) reveals a more pronounced enhancement in image quality compared to the single-view case. As the number of compound views grows from one to 4, 12, and 36, the reconstructed B/A maps exhibit a reduction in variability and a sharper delineation of the inclusion boundaries.

Although the B/A values remain higher compared to the ground truth (dashed lines), the reconstructions exhibit improved spatial homogeneity and lower speckle variability, as depicted in Fig. 4.9.

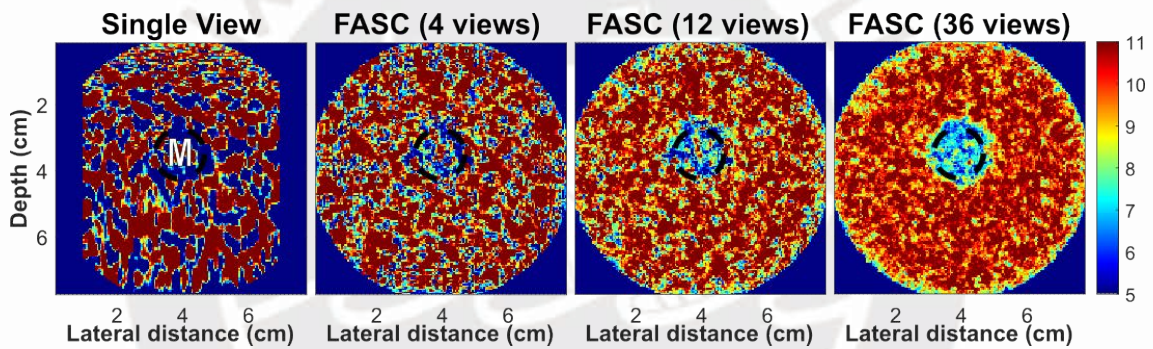


Figure 4.8: [Dataset V1a, $\theta = 90^\circ$] B/A maps of a single circular inclusion. Results are shown for both single view and FASC reconstructions with 4, 12 and 36 views. The transducer is adjacent to the phantom.

The quantitative results are consistent with the visual observations. As seen in Fig. 4.9, the \bar{x} and σ indicate that increasing the number of viewing angles leads to reduced variability in both the background and inclusion region. Similarly, the CNR and NRMSE metrics (Fig. 4.10) exhibit steady improvement with the application of FASC.

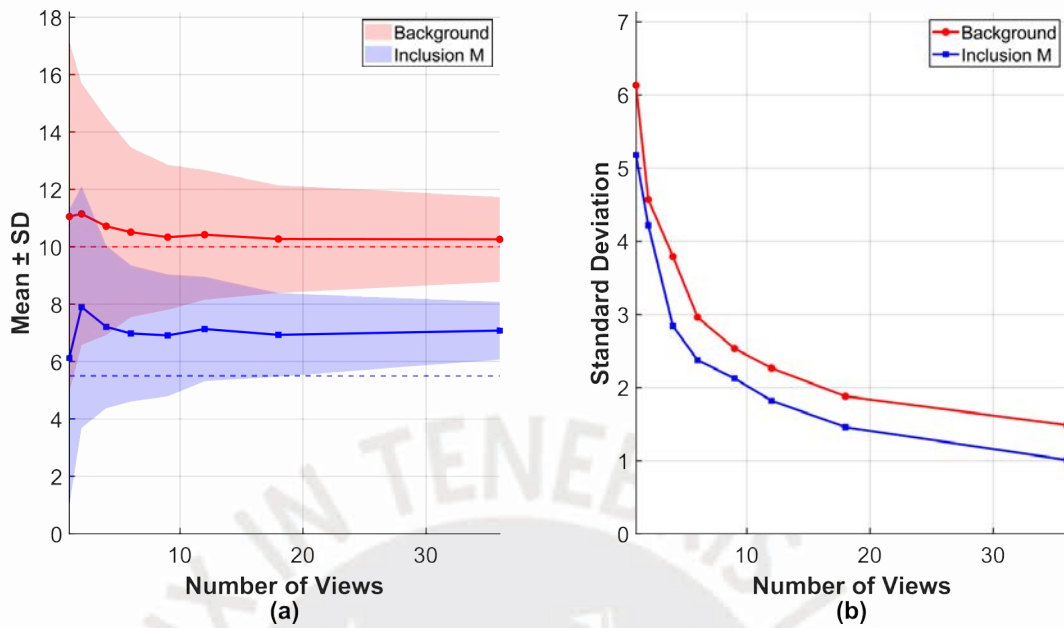


Figure 4.9: [Dataset V1a]: (a) Mean \pm SD. The horizontal dashed lines represent the ground truth values for the background (red), and inclusion M (blue). (b) Standard Deviation.

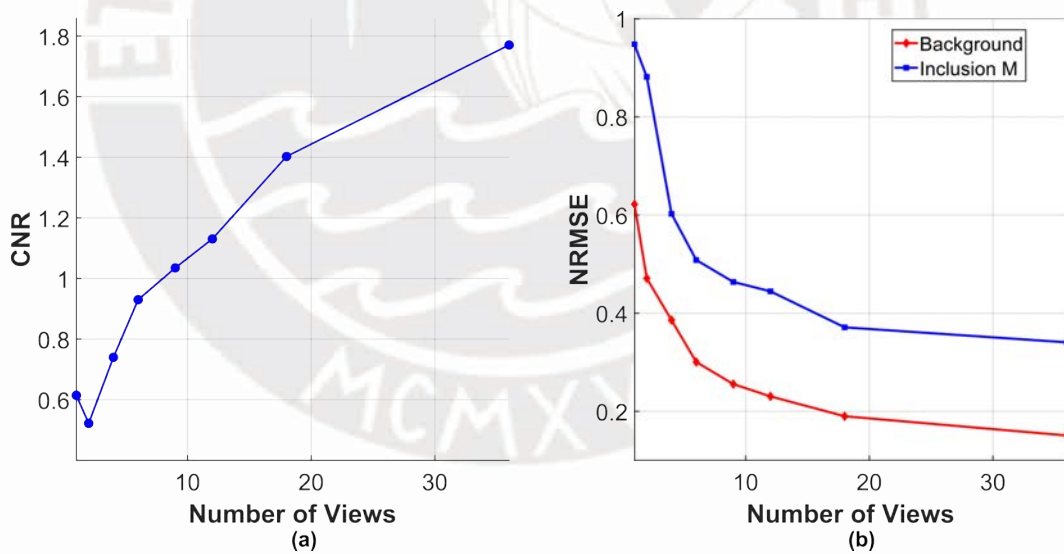


Figure 4.10: [Dataset V1a]: (a) CNR. (b) NRMSE.

For the single circular inclusions in V1a1–a4, the FASC reconstructions (Fig. 4.11) demonstrate that the benefits of FASC persist even as the inclusion diameter decreases. Across all cases, there are noticeable improvements in image quality relative to the single-view results.

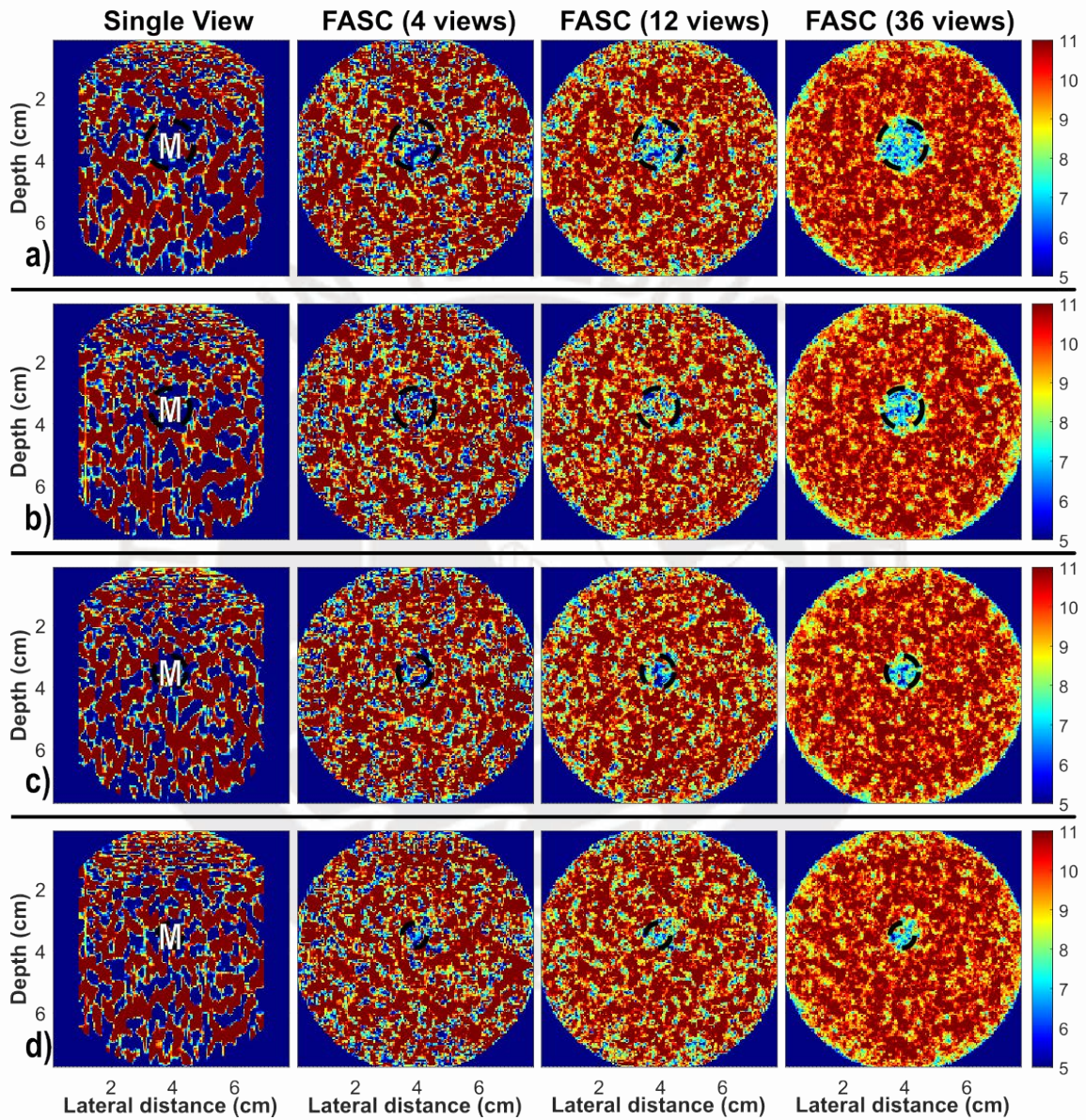


Figure 4.11: [Dataset V1a1-a4, $\theta = 90^\circ$] *B/A* maps of a single circular inclusion. Results are shown for both single view and FASC reconstructions with 4, 12 and 36 views. (a) $d = 0.875$ cm, (b) $d = 0.750$ cm, (c) $d = 0.625$ cm, and (d) $d = 0.500$ cm. The transducer is adjacent to the phantom.

As seen in Fig. 4.12, increasing the number of views improves NRMSE performance, indicating that FASC provides accurate and stable reconstructions across different inclusion sizes.

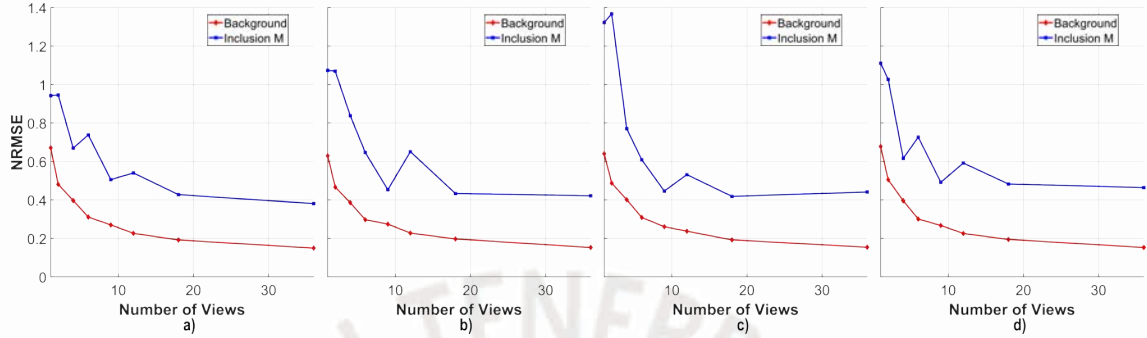


Figure 4.12: [Dataset V1a1-a4]: NRMSE (a) $d = 0.875$ cm, (b) $d = 0.750$ cm, (c) $d = 0.625$ cm, and (d) $d = 0.500$ cm.

For the single circular inclusion in V1b, the FASC reconstructions (Fig. 4.13) exhibit similar trends to those observed in V1a, despite the transducer being positioned 1 cm away from the phantom surface.

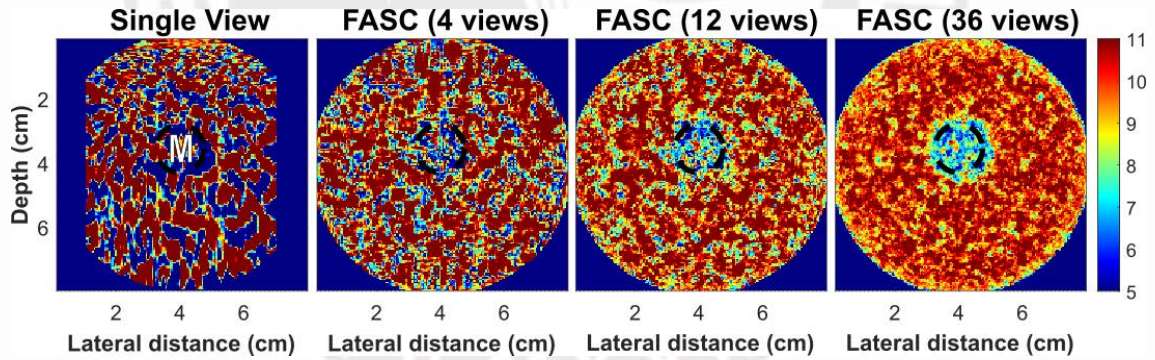


Figure 4.13: [Dataset V1b, $\theta = 90^\circ$] B/A maps of a single circular inclusion. Results are shown for both single view and FASC reconstructions with 4, 12 and 36 views. The transducer is positioned 1 cm away from the phantom.

In Fig. 4.14, the mean and standard deviation indicate a clear reduction in variability within both the background and inclusion regions as the number of viewing angles increases. Likewise, the CNR and NRMSE metrics (Fig. 4.15) denote improvement, confirming the method remains effective even when the transducer is placed 1 cm away from the phantom.

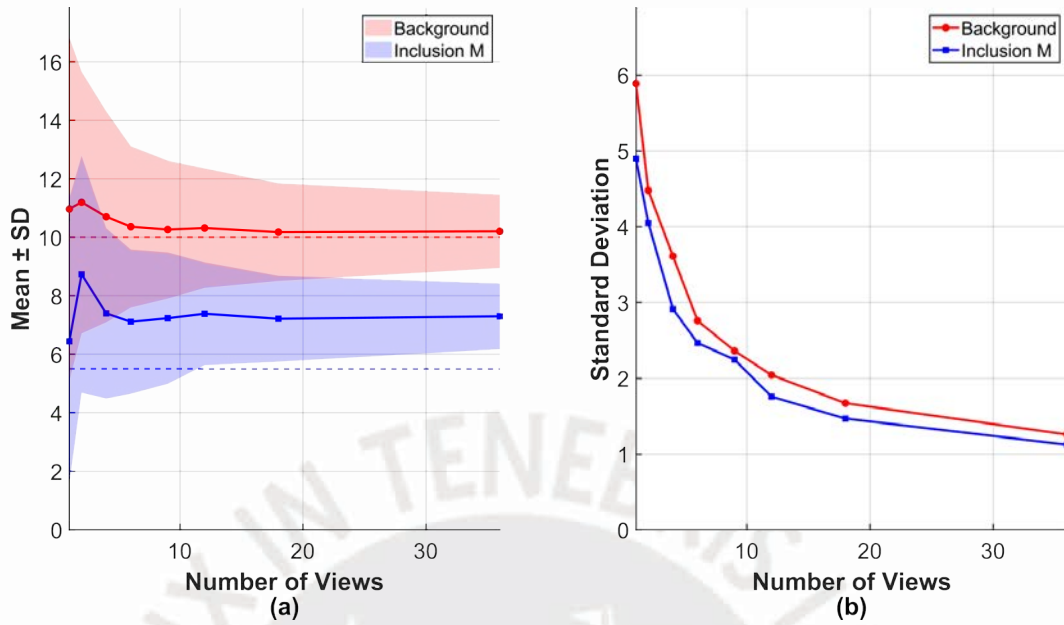


Figure 4.14: [Dataset V1b]: (a) Mean \pm SD. The horizontal dashed lines represent the ground truth values for the background (red), and inclusion M (blue). (b) Standard Deviation.

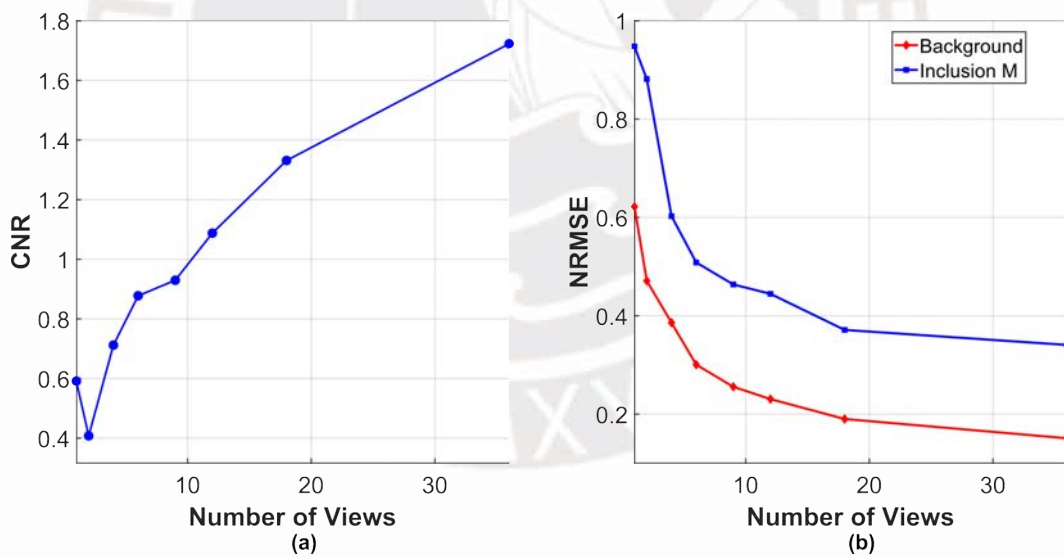


Figure 4.15: [Dataset V1b]: (a) CNR. (b) NRMSE.

4.2.3. Dataset versions: V3a & V3b

For the multi-inclusion case in V3a, the reconstructions (Fig. 4.16) further demonstrate the advantages of FASC in more complex configurations. The reconstructed B/A maps show reduced variability and a more homogeneous background compared to the single-view results, as the number of viewing angles rises from one to 4, 12, and 36. Despite the proximity B/A value of inclusion P to the surrounding background, which diminishes its visual contrast, the overall spatial uniformity and delineation of inclusions M and N improve noticeably with additional views.

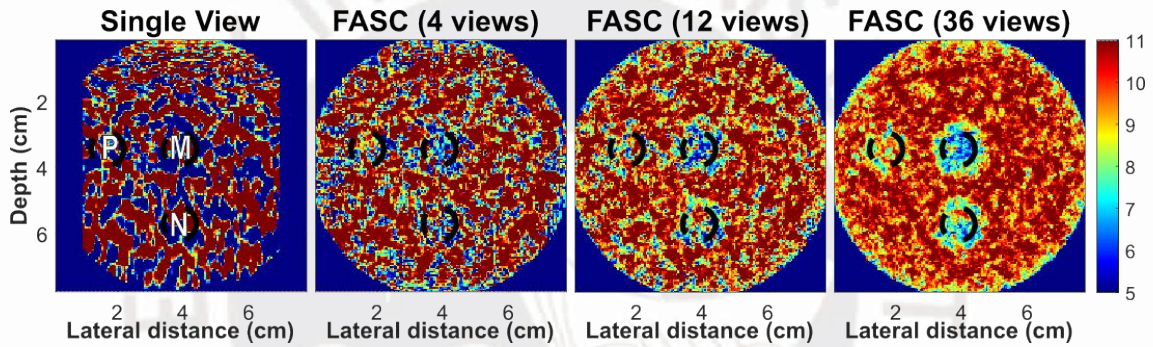


Figure 4.16: [Dataset V3a, $\theta = 90^\circ$] B/A maps of a single circular inclusion. Results are shown for both single view and FASC reconstructions with 4, 12 and 36 views. The transducer is adjacent to the phantom.

The quantitative analysis supports these visual observations. As shown in Fig. 4.17, the \bar{x} and σ trends converge progressively as the number of views increases, reflecting reduced variability across both inclusions and background regions. Similarly, the CNR and NRMSE metrics (Fig. 4.18) exhibit steady enhancement, confirming that FASC remains useful even in the presence of multiple inclusions.

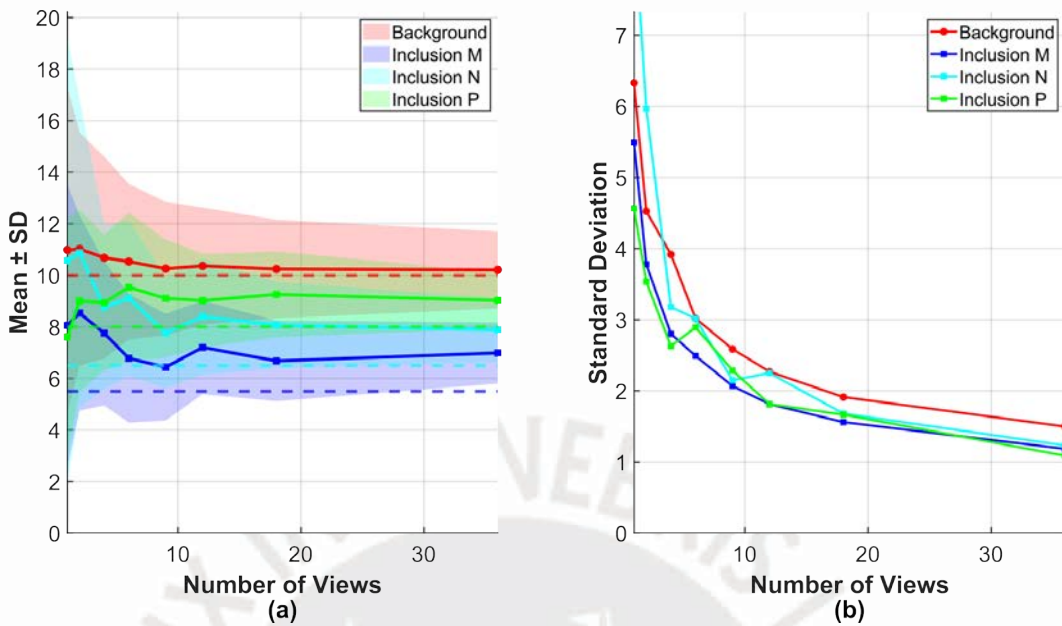


Figure 4.17: [Dataset V3a]: (a) Mean \pm SD. The horizontal dashed lines represent the ground truth values for the background (red) and inclusions M (blue), N (cyan), and P (green). (b) Standard Deviation.

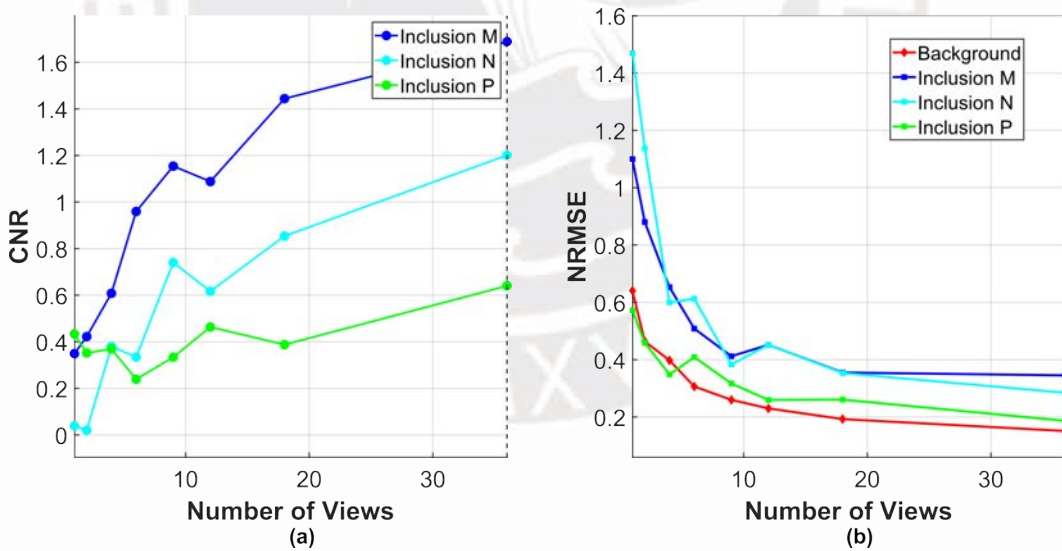


Figure 4.18: [Dataset V3a]: (a) CNR. (b) NRMSE.

For the multi-inclusion configuration in V3b, the FASC reconstructions (Fig. 4.19) exhibit a behavior similar to those observed in V3a, despite the transducer being positioned 1 cm away from the phantom surface. Although the increased propagation distance slightly reduces the visual contrast of inclusion P, given its proximity B/A value to the background, the delineation of inclusions M and N becomes clearer, and the overall image coherence continues to improve as the number of views increases.

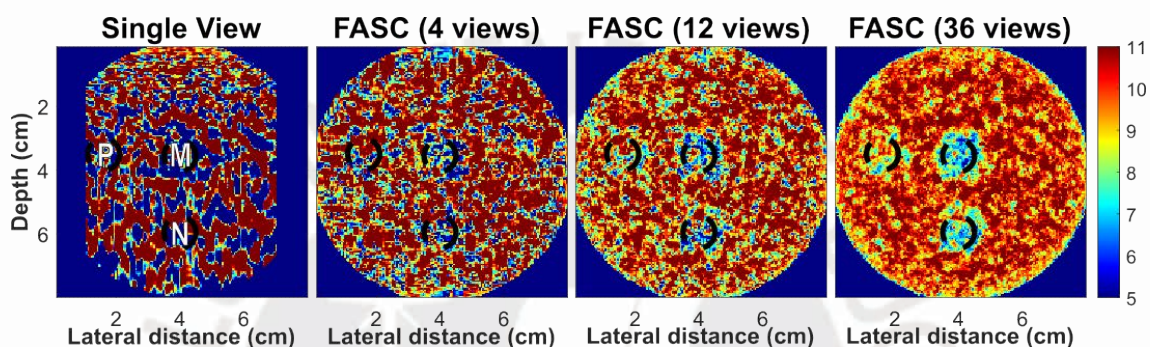


Figure 4.19: [Dataset V3b, $\theta = 90^\circ$] B/A maps of a single circular inclusion. Results are shown for both single view and FASC reconstructions with 4, 12 and 36 views. The transducer is positioned 1 cm away from the phantom.

Quantitative results support these visual findings. Fig. 4.20, shows that increasing the number of viewing angles reduces variability in both inclusions and background, while the CNR and NRMSE metrics (Fig. 4.21) improve consistently, verifying that FASC preserves its reconstruction accuracy and robustness even when there are multiple inclusions, and the transducer is placed 1 cm away from the phantom.

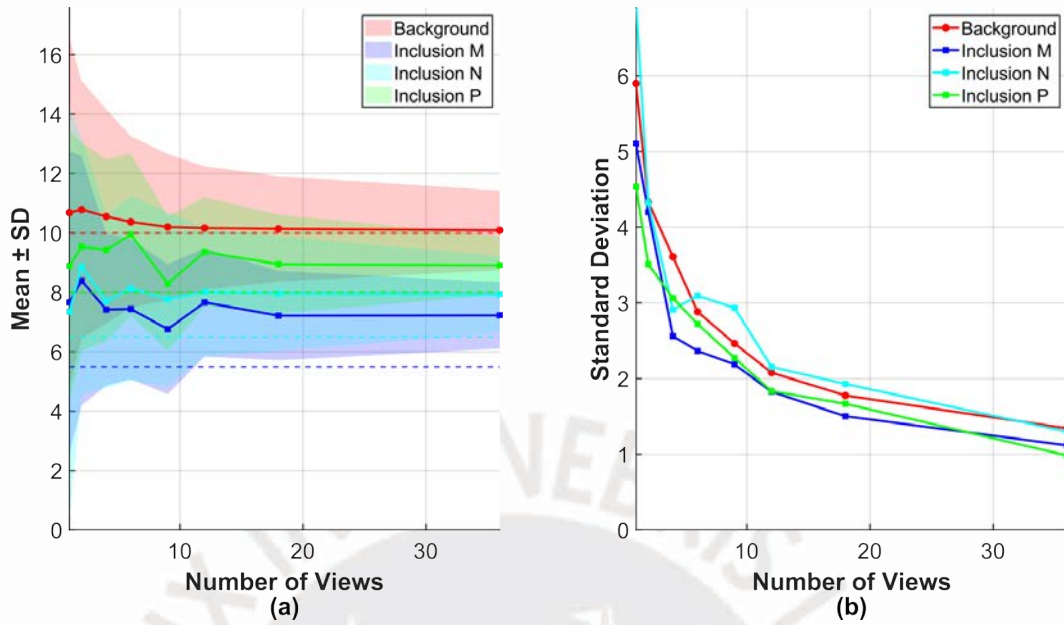


Figure 4.20: [Dataset V3b]: (a) Mean \pm SD. The horizontal dashed lines represent the ground truth values for the background (red) and inclusions M (blue), N (cyan), and P (green). (b) Standard Deviation.

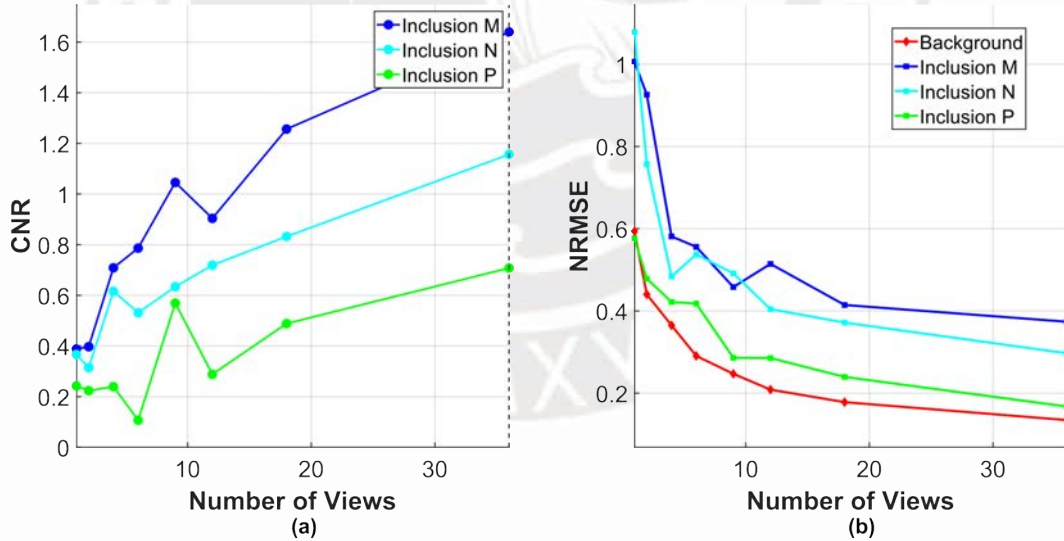


Figure 4.21: [Dataset V3b]: (a) CNR. (b) NRMSE.

4.3. Impact of the regularization parameter μ on reconstruction performance

This section examines the impact of μ on the performance of the FASC reconstruction framework. In the case of FASC with TV regularization, the influence of μ was systematically analyzed over the discrete set $[10^{-4}, 10^{-3}, 10^{-2}, 10^{-1}, 10^0, 10^1, 10^2, 10^3]$. The following analysis evaluates how different μ values affect quantitative metrics.

4.3.1. Dataset versions: V1a & V1b

For the V1a dataset, as μ increases from lower values to 10^{-1} , both the \bar{x} and σ of the reconstructed B/A estimates decrease and stabilize, denoting reduced variability (Fig 4.22).

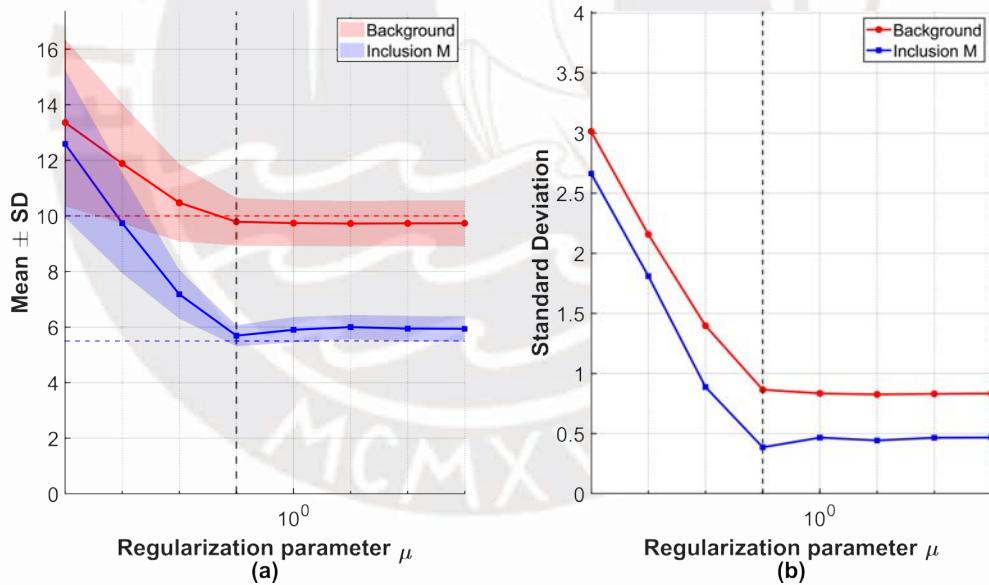


Figure 4.22: [Dataset V1a]: (a) Mean \pm SD. The horizontal dashed lines represent the ground truth values for the background (red), and inclusion M (blue). (b) Standard Deviation.

In parallel, the CNR reaches its maximum, and the NRMSE for both the background and inclusion achieves its minimum at $\mu = 10^{-1}$, as shown in Fig. 4.23.

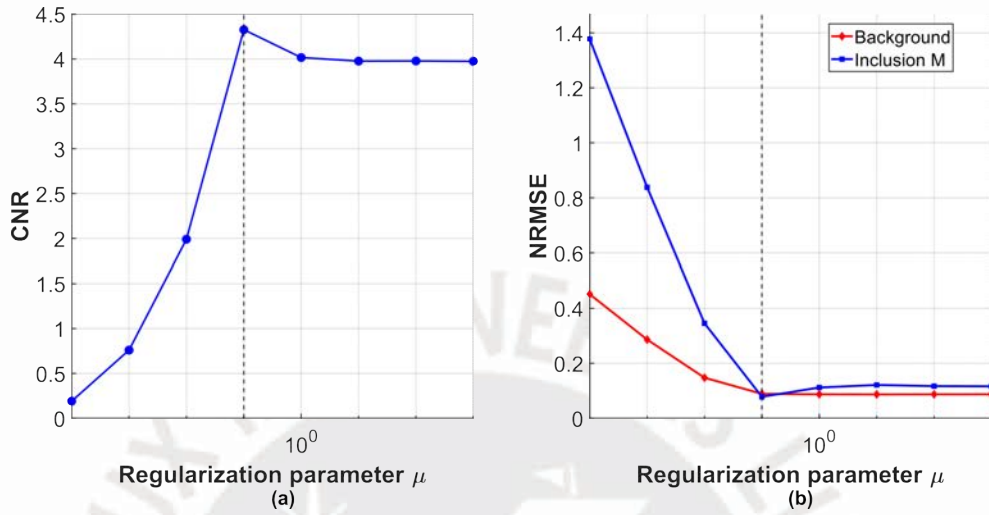


Figure 4.23: [Dataset V1a]: (a) CNR. (b) NRMSE.

For V1b, where the transducer is placed 1 cm away from the phantom, similar behavior was observed. At $\mu = 10^{-1}$, both the \bar{x} and σ decrease and stabilize (Fig 4.24).

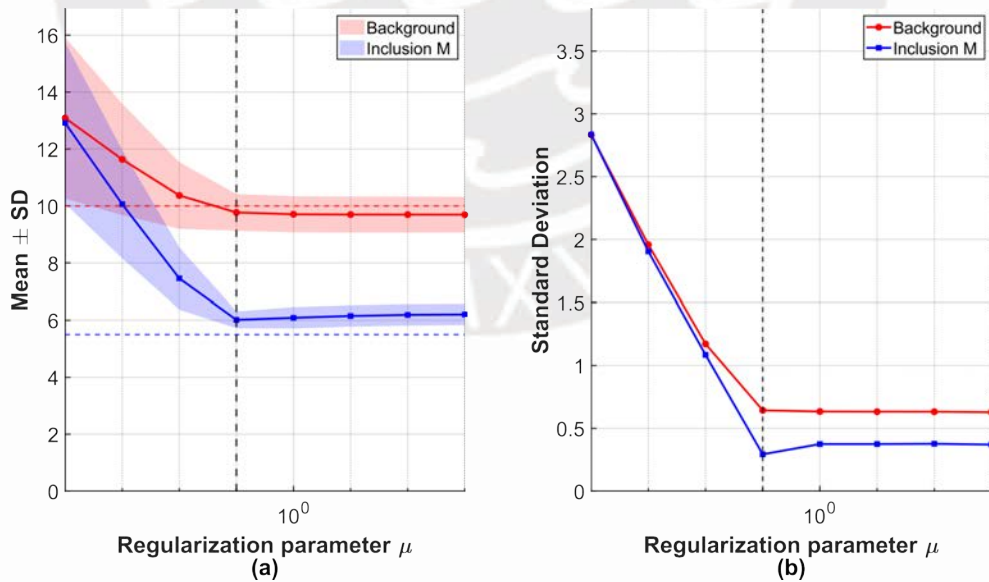


Figure 4.24: [Dataset V1b]: (a) Mean \pm SD. The horizontal dashed lines represent the ground truth values for the background (red), and inclusion M (blue). (b) Standard Deviation.

Similarly as in V1a, the CNR reaches its maximum, and the NRMSE for both the background and inclusion achieves its minimum at $\mu = 10^{-1}$, as shown in Fig. 4.25.

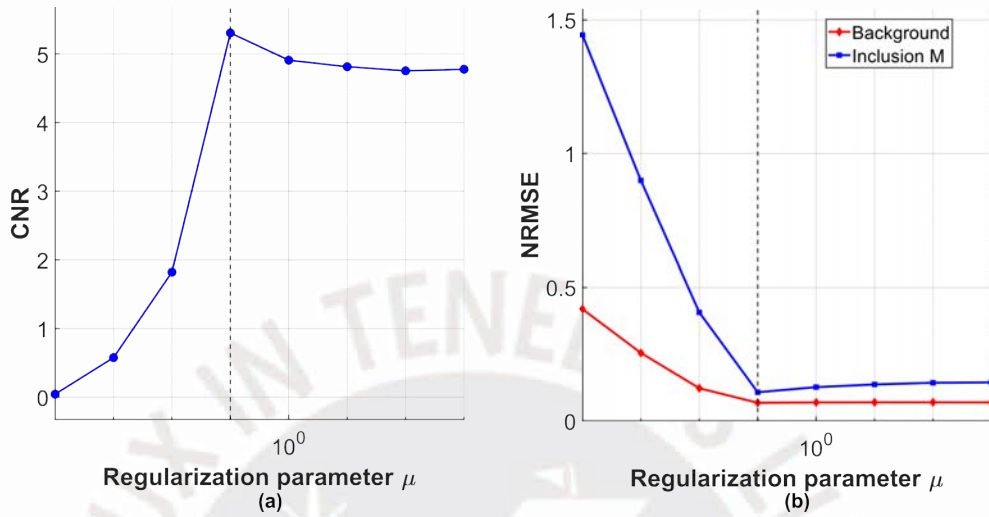


Figure 4.25: [Dataset V1b]: (a) CNR. (b) NRMSE.

Importantly, this trend was consistent across all simulations, where $\mu = 10^{-1}$ systematically provided the best balance between variance reduction, inclusion contrast, and spatial uniformity.

4.4. B/A estimation comparison

This section is a comparison of the different reconstruction approaches applied for B/A estimation. An analysis focused on assessing how FASC and TV regularization individually and jointly influence the accuracy, contrast, and spatial uniformity of the reconstructed B/A maps.

4.4.1. Dataset versions: V1star

For dataset V1star, Fig. 4.26 exhibits the reconstructed B/A maps obtained using different reconstruction strategies. In both, SV, and SV + TV approaches, (b, d), the inclusion can not be discerned due to high variability and poor spatial coherence. When FASC, c), is introduced the spatial uniformity improves, allowing to distinguish the inclusion. The combination of FASC + TV, e), delivers the most accurate and visually coherent B/A map, closely matching the ground truth.

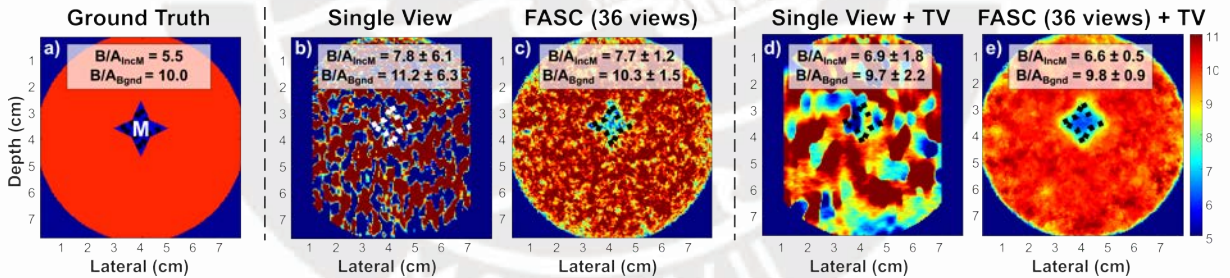


Figure 4.26: B/A maps for simulation V1star: Columns exhibit the Ground Truth, Single View, FASC (36 views), Single View + TV, FASC (36 views) + TV reconstructions.

The NRMSE values for the star-cross shaped inclusion were 1.19 for the SV, 0.46 for FASC, and 0.23 for FASC + TV. As summarized in Table 4.1, the CNR values further highlight this improvement, with FASC + TV achieving the highest contrast (3.22), followed by FASC (1.36) and SV (0.39).

Table 4.1: Statistics for B/A maps of Simulation V1star

Region	Single View			FASC (36 views)		
	$\bar{x} \pm \sigma$	NRMSE	CNR	$\bar{x} \pm \sigma$	NRMSE	CNR
Inc. M	7.79 ± 6.13	1.19	0.39	7.73 ± 1.21	0.46	1.36
Back.	11.19 ± 6.33	0.64		10.34 ± 1.49	0.15	
Region	Single View + TV			FASC (36 views) + TV		
	$\bar{x} \pm \sigma$	NRMSE	CNR	$\bar{x} \pm \sigma$	NRMSE	CNR
Inc. M	6.86 ± 1.77	0.41	0.99	6.66 ± 0.47	0.23	3.22
Back.	9.66 ± 2.21	0.22		9.81 ± 0.86	0.09	

4.4.2. Dataset versions: V1a & V1b

For datasets V1a and V1b, Fig. 4.27 presents the reconstructed B/A maps obtained using different reconstruction approaches. In both SV and SV + TV methods, (b, d, g, i), the inclusion can not be discern due to high variability and poor spatial coherence. When FASC is applied to SV, (c, h), spatial uniformity improves, allowing to perceive the inclusion. The combined FASC + TV approach, (e, j), yields the most accurate and visually consistent B/A map, closely resembling the ground truth.

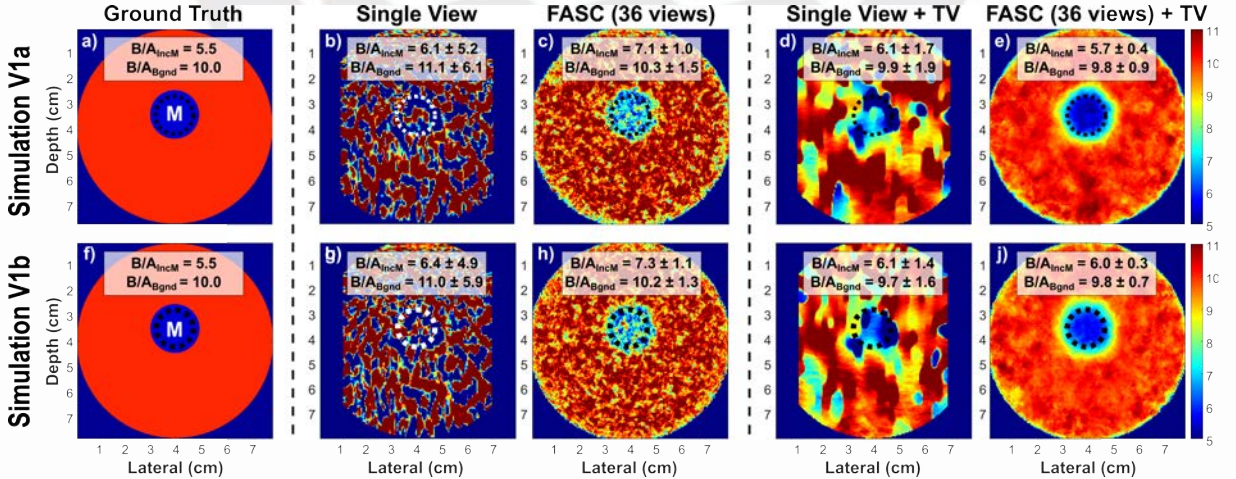


Figure 4.27: B/A maps for simulation V1a & V1b: Columns exhibit the Ground Truth, Single View, FASC (36 views), Single View + TV, FASC (36 views) + TV reconstructions.

As shown in Tables 4.2 and 4.3, both datasets exhibit consistent behavior. For V1a, the NRMSE values for the inclusion decrease from 0.95 (SV) to 0.34 (FASC) and 0.08 (FASC + TV), while the CNR increases from 0.61 to 1.77 and 4.33, respectively. Similarly, for V1b, the inclusion NRMSE decreases from 0.91 to 0.39 and 0.11, and the CNR rises from 0.59 to 1.72 and 5.14.

Table 4.2: Statistics for *B/A* maps of Simulation V1a

Region	Single View			FASC (36 views)		
	$\bar{x} \pm \sigma$	NRMSE	CNR	$\bar{x} \pm \sigma$	NRMSE	CNR
Inc. M	6.12 ± 5.18	0.95	0.61	7.08 ± 1.01	0.34	1.77
Back.	11.05 ± 6.13	0.62		10.26 ± 1.49	0.15	
Region	Single View + TV			FASC (36 views) + TV		
	$\bar{x} \pm \sigma$	NRMSE	CNR	$\bar{x} \pm \sigma$	NRMSE	CNR
Inc. M	6.05 ± 1.66	0.32	1.54	5.69 ± 0.39	0.08	4.33
Back.	9.90 ± 1.88	0.19		9.79 ± 0.86	0.09	

Despite the 1 cm separation between the transducer and the phantom in V1b, FASC + TV consistently delivers the most accurate and visually coherent *B/A* reconstructions.

Table 4.3: Statistics for *B/A* maps of Simulation V1b

Region	Single View			FASC (36 views)		
	$\bar{x} \pm \sigma$	NRMSE	CNR	$\bar{x} \pm \sigma$	NRMSE	CNR
Inc. M	6.44 ± 4.89	0.91	0.59	7.29 ± 1.12	0.39	1.72
Back.	10.97 ± 5.89	0.60		10.20 ± 1.26	0.13	
Region	Single View + TV			FASC (36 views) + TV		
	$\bar{x} \pm \sigma$	NRMSE	CNR	$\bar{x} \pm \sigma$	NRMSE	CNR
Inc. M	6.10 ± 1.45	0.29	1.68	6.04 ± 0.30	0.11	5.14
Back.	9.75 ± 1.62	0.16		9.76 ± 0.66	0.07	

4.4.3. Dataset versions: V3a & V3b

For datasets V3a and V3b, Fig. 4.28 presents the reconstructed B/A maps obtained using different reconstruction strategies. In both the SV and SV + TV approaches, (b, d, g, i), the inclusions can not be distinguish due to strong variability and poor spatial coherence. When FASC is applied to SV (c, h), spatial uniformity improves, allowing inclusions M and N to be more clearly identified. The combined FASC + TV configuration, (e, j), yields the most accurate and visually consistent reconstructions, closely matching the ground truth across all inclusions.

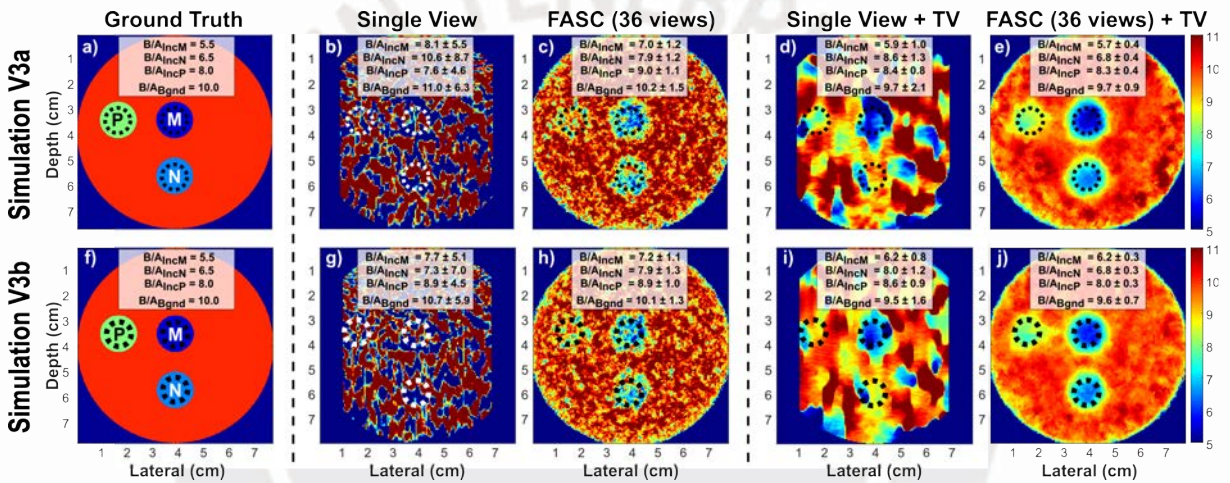


Figure 4.28: B/A maps for simulation V3a & V3b: Columns exhibit the Ground Truth, Single View, FASC (36 views), Single View + TV, FASC (36 views) + TV reconstructions.

As summarized in Tables 4.4 and 4.5, for V3a, the average NRMSE values for inclusions and background decrease from 0.94 (SV) to 0.24 (FASC) and further to 0.07 (FASC + TV), while the average CNR increases from 0.27 (SV) to 1.18 (FASC) and 2.8 (FASC + TV). Similarly, for V3b, the average NRMSE values drop from 0.81 (SV) to 0.24 (FASC) and 0.08 (FASC + TV), while the average CNR increases from 0.27 (SV) to 1.18 (FASC) and 3.28 (FASC + TV).

Table 4.4: Statistics for *B/A* maps of Simulation V3a

Region	Single View			FASC (36 views)		
	$\bar{x} \pm \sigma$	NRMSE	CNR	$\bar{x} \pm \sigma$	NRMSE	CNR
Inc. M	8.05 ± 5.49	1.09	0.35 0.04 0.43	6.99 ± 1.18	0.35	1.69 1.20 0.64
Inc. N	10.56 ± 8.65	1.47		7.88 ± 1.23	0.28	
Inc. P	7.60 ± 4.56	0.57		9.02 ± 1.09	0.19	
Back.	10.98 ± 6.33	0.64		10.21 ± 1.50	0.15	
Region	Single View + TV			FASC (36 views) + TV		
	$\bar{x} \pm \sigma$	NRMSE	CNR	$\bar{x} \pm \sigma$	NRMSE	CNR
Inc. M	5.92 ± 0.97	0.19	1.65 0.47 0.60	5.73 ± 0.40	0.08	4.00 2.95 1.45
Inc. N	8.55 ± 1.26	0.37		6.82 ± 0.35	0.07	
Inc. P	8.35 ± 0.80	0.11		8.28 ± 0.36	0.05	
Back.	9.67 ± 2.06	0.21		9.68 ± 0.90	0.09	

Even with a 1 cm gap between the transducer and the phantom in V3b, the FASC + TV approach continues to provide the most accurate and visually consistent *B/A* reconstructions.

Table 4.5: Statistics for *B/A* maps of Simulation V3b

Region	Single View			FASC (36 views)		
	$\bar{x} \pm \sigma$	NRMSE	CNR	$\bar{x} \pm \sigma$	NRMSE	CNR
Inc. M	7.66 ± 5.10	1.01	0.39 0.37 0.24	7.23 ± 1.12	0.37	1.64 1.16 0.71
Inc. N	7.34 ± 6.97	1.08		7.93 ± 1.29	0.29	
Inc. P	8.88 ± 4.53	0.58		8.91 ± 0.98	0.17	
Back.	10.68 ± 5.89	0.59		10.09 ± 1.34	0.13	
Region	Single View + TV			FASC (36 views) + TV		
	$\bar{x} \pm \sigma$	NRMSE	CNR	$\bar{x} \pm \sigma$	NRMSE	CNR
Inc. M	6.18 ± 0.80	0.19	1.83 0.77 0.48	6.19 ± 0.29	0.14	4.31 3.52 2.00
Inc. N	7.97 ± 1.22	0.29		6.79 ± 0.32	0.07	
Inc. P	8.63 ± 0.86	0.13		8.03 ± 0.27	0.03	
Back.	9.53 ± 1.64	0.17		9.59 ± 0.73	0.08	

Conclusions

In this study, numerical breast-like phantoms were successfully simulated using the k-Wave toolbox, allowing the evaluation of the B/A estimation framework under various configurations, including complex multi-inclusion scenarios and varying transducer-phantom distances.

The combination of FASC with the depletion method framework successfully produced B/A maps with greater spatial coherence, reduced variability, and clearer inclusion edges compared to single-view reconstructions. The approach proved effective even under challenging conditions, such as anisotropic inclusion geometry in V1star, decreased inclusion diameter in V1a1-a4, and multiple-inclusion setups in V3a and V3b, yielding stable B/A values that closely approximated the ground truth.

While FASC alone displayed improvements in spatial coherence and reduced variance, its precision was limited in phantoms where B/A values between inclusions and background were similar (inclusion P in V3a and V3b). Incorporating an optimal TV regularization parameter effectively addressed it, by promoting spatial smoothness and preserving structural edges.

Quantitatively, the FASC + TV configuration achieved the lowest NRMSE and highest CNR values, providing reconstructions that closely matched the ground truth B/A maps. This approach proved robustness even under challenging acquisition geometries, such as the 1 cm transducer-phantom distance separation.

Recommendations

While the present study demonstrated the feasibility and effectiveness of the FASC framework combined with TV regularization for *B/A* imaging as seen in Chapter 4.4, several aspects can be explored and refined:

- Extension beyond *in silico* validation: Future studies should extend this work to experimental and *in vivo* validations, considering the effects of tissue heterogeneity, motion, and acoustic attenuation, which may introduce artifacts or reduce inclusion delineation.
- Adaptive parameter optimization: The method's performance is influenced by the selection of the regularization parameter (μ) and the number of viewing angles. Adopting a data-driven approach to automatically adjust μ and determine the optimal number of views could improve reconstruction stability and minimize manual parameter tuning.

Bibliography

- [1] E. D. Miranda, R. Lavarello, and A. Coila, “Enhancing breast nonlinearity parameter imaging using full angular spatial compounding,” in *2025 IEEE International Ultrasonics Symposium (IUS)*. IEEE, 2025, pp. 1–4.
- [2] C. D. Lehman, A. Y. Lee, and C. I. Lee, “Imaging management of palpable breast abnormalities,” *American journal of roentgenology*, vol. 203, no. 5, pp. 1142–1153, 2014.
- [3] N. Houssami, M. Cheung, and J. M. Dixon, “Fibroadenoma of the breast.” *The Medical Journal of Australia*, vol. 174, no. 4, pp. 185–188, 2001.
- [4] M. Guray and A. A. Sahin, “Benign breast diseases: classification, diagnosis, and management,” *The oncologist*, vol. 11, no. 5, pp. 435–449, 2006.
- [5] E. Boakes, A. Woods, N. Johnson, and N. Kadoglou, “Breast infection: a review of diagnosis and management practices,” *European journal of breast health*, vol. 14, no. 3, p. 136, 2018.
- [6] D. J. Marchant, “Inflammation of the breast.” *Obstetrics and Gynecology Clinics of North America*, vol. 29, no. 1, pp. 89–102, 2002.

- [7] R. C. Richie and J. O. Swanson, "Breast cancer: a review of the literature," *JOURNAL OF INSURANCE MEDICINE-NEW YORK THEN DENVER*-, vol. 35, no. 2, pp. 85–101, 2003.
- [8] S. Libson and M. Lippman, "A review of clinical aspects of breast cancer," *International review of psychiatry*, vol. 26, no. 1, pp. 4–15, 2014.
- [9] H. G. Nasief, I. M. Rosado-Mendez, J. A. Zagzebski, and T. J. Hall, "Acoustic properties of breast fat," *Journal of Ultrasound in Medicine*, vol. 34, no. 11, pp. 2007–2016, 2015.
- [10] E. D. Pisano and M. J. Yaffe, "Digital mammography," *Radiology*, vol. 234, no. 2, pp. 353–362, 2005.
- [11] A. Athanasiou, A. Tardivon, L. Ollivier, F. Thibault, C. El Khoury, and S. Neuenschwander, "How to optimize breast ultrasound," *European journal of radiology*, vol. 69, no. 1, pp. 6–13, 2009.
- [12] J. Mamou and M. L. Oelze, *Quantitative ultrasound in soft tissues*. Springer, 2013.
- [13] F. Foster, M. Strban, and G. Austin, "The ultrasound macroscope: initial studies of breast tissue," *Ultrasonic imaging*, vol. 6, no. 3, pp. 243–261, 1984.
- [14] F. d'Astous and F. Foster, "Frequency dependence of ultrasound attenuation and backscatter in breast tissue," *Ultrasound in medicine & biology*, vol. 12, no. 10, pp. 795–808, 1986.
- [15] L. Landini, R. Sarnelli, M. Salvadori, and F. Squartini, "Orientation and frequency dependence of backscatter coefficient in normal and pathological breast tissues," *Ultrasound in medicine & biology*, vol. 13, no. 2, pp. 77–83, 1987.

- [16] L. Landini and R. Sarnelli, "Evaluation of the attenuation coefficients in normal and pathological breast tissue," *Medical and Biological Engineering and Computing*, vol. 24, pp. 243–247, 1986.
- [17] A. Panfilova, R. J. van Sloun, H. Wijkstra, O. A. Sapozhnikov, and M. Mischi, "A review on B/A measurement methods with a clinical perspective," *The Journal of the Acoustical Society of America*, vol. 149, no. 4, pp. 2200–2237, 2021.
- [18] W. Law, L. Frizzell, and F. Dunn, "Determination of the nonlinearity parameter B/A of biological media," *Ultrasound in medicine & biology*, vol. 11, no. 2, pp. 307–318, 1985.
- [19] R. L. Errabolu, C. M. Sehgal, R. C. Bahn, and J. F. Greenleaf, "Measurement of ultrasonic nonlinear parameter in excised fat tissues," *Ultrasound in medicine & biology*, vol. 14, no. 2, pp. 137–146, 1988.
- [20] A. L. Coila Pacompia, "Quantitative ultrasound and the effects of acoustic nonlinearity," 2022.
- [21] R. T. Beyer, "Parameter of nonlinearity in fluids," *The Journal of the Acoustical Society of America*, vol. 32, no. 6, pp. 719–721, 1960.
- [22] S. Saito, "Measurement of the acoustic nonlinearity parameter in liquid media using focused ultrasound," *The Journal of the Acoustical Society of America*, vol. 93, no. 1, pp. 162–172, 1993.
- [23] X. Liu, X. Gong, C. Yin, J. Li, and D. Zhang, "Noninvasive estimation of temperature elevations in biological tissues using acoustic nonlinearity parameter imaging," *Ultrasound in medicine & biology*, vol. 34, no. 3, pp. 414–424, 2008.

- [24] Y. Lu, X. Liu, X. Gong, and D. Zhang, "Relationship between the temperature and the acoustic nonlinearity parameter in biological tissues," *Chinese Science Bulletin*, vol. 49, pp. 2360–2363, 2004.
- [25] D. Zhang, X.-f. Gong, and X. Chen, "Experimental imaging of the acoustic nonlinearity parameter B/A for biological tissues via a parametric array," *Ultrasound in medicine & biology*, vol. 27, no. 10, pp. 1359–1365, 2001.
- [26] X. Gong, D. Zhang, J. Liu, H. Wang, Y. Yan, and X. Xu, "Study of acoustic nonlinearity parameter imaging methods in reflection mode for biological tissues," *The Journal of the Acoustical Society of America*, vol. 116, no. 3, pp. 1819–1825, 2004.
- [27] X. Gong, X. Liu, D. Zhang *et al.*, "Influence of tissue composition and structural features of biological media in the ultrasonic nonlinearity parameter," *Chin. J. Acoust.*, vol. 12, no. 3, pp. 265–270, 1993.
- [28] X.-f. Gong, Z.-m. Zhu, T. Shi, and J.-h. Huang, "Determination of the acoustic nonlinearity parameter in biological media using FAIS and ITD methods," *The Journal of the Acoustical Society of America*, vol. 86, no. 1, pp. 1–5, 1989.
- [29] D. Zhang and X.-F. Gong, "Experimental investigation of the acoustic nonlinearity parameter tomography for excised pathological biological tissues," *Ultrasound in medicine & biology*, vol. 25, no. 4, pp. 593–599, 1999.
- [30] C. M. Sehgal, R. C. Bahn, and J. F. Greenleaf, "Measurement of the acoustic nonlinearity parameter B/A in human tissues by a thermodynamic method," *The Journal of the Acoustical Society of America*, vol. 76, no. 4, pp. 1023–1029, 1984.

- [31] C. Sehgal, G. Brown, R. Bahn, and J. F. Greenleaf, "Measurement and use of acoustic nonlinearity and sound speed to estimate composition of excised livers," *Ultrasound in medicine & biology*, vol. 12, no. 11, pp. 865–874, 1986.
- [32] S. F. Reis *et al.*, "Characterisation of biological tissue: measurement of acoustic properties for Ultrasound Therapy," Ph.D. dissertation, 2013.
- [33] S. Yongchen, D. Yanwu, T. Jie, and T. Zhensheng, "Ultrasonic propagation parameters in human tissues," in *IEEE 1986 Ultrasonics Symposium*. IEEE, 1986, pp. 905–908.
- [34] M. L. Oelze and J. Mamou, "Review of quantitative ultrasound: Envelope statistics and backscatter coefficient imaging and contributions to diagnostic ultrasound," *IEEE transactions on ultrasonics, ferroelectrics, and frequency control*, vol. 63, no. 2, pp. 336–351, 2016.
- [35] A. Coila and M. L. Oelze, "Effects of acoustic nonlinearities on the ultrasonic backscatter coefficient estimation," *The Journal of the Acoustical Society of America*, vol. 146, no. 1, pp. 85–94, 2019.
- [36] S. C. Lin, E. Heba, T. Wolfson, B. Ang, A. Gamst, A. Han, J. W. Erdman Jr, W. D. O'Brien Jr, M. P. Andre, C. B. Sirlin *et al.*, "Noninvasive diagnosis of nonalcoholic fatty liver disease and quantification of liver fat using a new quantitative ultrasound technique," *Clinical Gastroenterology and Hepatology*, vol. 13, no. 7, pp. 1337–1345, 2015.
- [37] R. J. Miller, A. Han, J. W. Erdman Jr, M. A. Wallig, and W. D. O'Brien Jr, "Quantitative ultrasound and the pancreas: Demonstration of early detection capability," *Journal of Ultrasound in Medicine*, vol. 38, no. 8, pp. 2093–2102, 2019.
- [38] L. Sannachi, H. Tadayyon, A. Sadeghi-Naini, W. Tran, S. Gandhi, F. Wright, M. Oelze, and G. Czarnota, "Non-invasive evaluation of breast cancer response to chemotherapy using

- quantitative ultrasonic backscatter parameters,” *Medical image analysis*, vol. 20, no. 1, pp. 224–236, 2015.
- [39] R. J. Lavarello, G. Ghoshal, and M. L. Oelze, “On the estimation of backscatter coefficients using single-element focused transducers,” *The Journal of the Acoustical Society of America*, vol. 129, no. 5, pp. 2903–2911, 2011.
- [40] X. Chen, D. Phillips, K. Q. Schwarz, J. G. Mottley, and K. J. Parker, “The measurement of backscatter coefficient from a broadband pulse-echo system: A new formulation,” *IEEE transactions on ultrasonics, ferroelectrics, and frequency control*, vol. 44, no. 2, pp. 515–525, 1997.
- [41] L. X. Yao, J. A. Zagzebski, and E. L. Madsen, “Backscatter coefficient measurements using a reference phantom to extract depth-dependent instrumentation factors,” *Ultrasonic imaging*, vol. 12, no. 1, pp. 58–70, 1990.
- [42] F. Duck, *Physical properties of tissues: a comprehensive reference book*. Academic press, 2013.
- [43] Y. Labyed and T. A. Bigelow, “A theoretical comparison of attenuation measurement techniques from backscattered ultrasound echoes,” *The Journal of the Acoustical Society of America*, vol. 129, no. 4, pp. 2316–2324, 2011.
- [44] R. Kuc and M. Schwartz, “Estimating the acoustic attenuation coefficient slope for liver from reflected ultrasound signals,” *IEEE Transactions on Sonics and Ultrasonics*, vol. 26, no. 5, pp. 353–361, 1979.
- [45] S. K. Jeon, J. M. Lee, I. Joo, J. H. Yoon, D. H. Lee, J. Y. Lee, and J. K. Han, “Prospective evaluation of hepatic steatosis using ultrasound attenuation imaging in patients with chronic liver disease with magnetic resonance imaging proton density fat fraction as the

- reference standard,” *Ultrasound in medicine & biology*, vol. 45, no. 6, pp. 1407–1416, 2019.
- [46] H. G. Nasief, I. M. Rosado-Mendez, J. A. Zagzebski, and T. J. Hall, “A quantitative ultrasound-based multi-parameter classifier for breast masses,” *Ultrasound in medicine & biology*, vol. 45, no. 7, pp. 1603–1616, 2019.
- [47] F. Deeba, M. Ma, M. Pesteie, J. Terry, D. Pugash, J. A. Hutcheon, C. Mayer, S. Salcudean, and R. Rohling, “Attenuation coefficient estimation of normal placentas,” *Ultrasound in medicine & biology*, vol. 45, no. 5, pp. 1081–1093, 2019.
- [48] A. Coila, J. Rouyer, O. Zenteno, A. Luchies, M. L. Oelze, and R. Lavarello, “Total attenuation compensation for backscatter coefficient estimation using full angular spatial compounding,” *Ultrasonics*, vol. 114, p. 106376, 2021.
- [49] O. Zenteno, A. Luchies, M. Oelze, and R. Lavarello, “Improving the quality of attenuation imaging using full angular spatial compounding,” in *2014 IEEE international ultrasonics symposium*. IEEE, 2014, pp. 2426–2429.
- [50] I. Akiyama, “Reflection mode measurement of nonlinearity parameter B/A,” in *AIP Conference Proceedings*, vol. 524, no. 1. American Institute of Physics, 2000, pp. 321–324.
- [51] Y. Fujii, N. Taniguchi, I. Akiyama, J.-W. Tsao, and K. Itoh, “A new system for in vivo assessment of the degree of nonlinear generation using the second harmonic component in echo signals,” *Ultrasound in medicine & biology*, vol. 30, no. 11, pp. 1511–1516, 2004.
- [52] R. Van Sloun, L. Demi, C. Shan, and M. Mischi, “Ultrasound coefficient of nonlinearity imaging,” *IEEE Transactions on Ultrasonics, Ferroelectrics, and Frequency Control*, vol. 62, no. 7, pp. 1331–1341, 2015.

- [53] F. Varray, J. Chenot, O. Basset, P. Tortoli, D. Melodelima, and C. Cachard, “Nonlinear parameter imaging to characterize HIFU ablation: Preliminary in vitro results in porcine liver,” in *2011 IEEE International Ultrasonics Symposium*. IEEE, 2011, pp. 1361–1363.
- [54] M. Toulemonde, F. Varray, O. Basset, P. Tortoli, and C. Cachard, “High frame rate compounding for nonlinear B/A parameter ultrasound imaging in echo mode—simulation results,” in *2014 IEEE International Conference on Acoustics, Speech and Signal Processing (ICASSP)*. IEEE, 2014, pp. 5153–5157.
- [55] A. Coila, A. Romero, E. A. Miranda, M. L. Oelze, and R. Lavarello, “Depletion of backscattered fundamental band signal for nonlinearity parameter imaging,” in *2023 IEEE International Ultrasonics Symposium (IUS)*. IEEE, 2023, pp. 1–4.
- [56] M. Nikoonahad and D. Liu, “Pulse-echo single frequency acoustic nonlinearity parameter B/A measurement,” *IEEE transactions on ultrasonics, ferroelectrics, and frequency control*, vol. 37, no. 3, pp. 127–134, 1990.
- [57] D. Liu and M. Nikoonahad, “Pulse-echo B/A measurement using variable amplitude excitation,” in *Proceedings., IEEE Ultrasonics Symposium.* IEEE, 1989, pp. 1047–1051.
- [58] J. Prince and J. Links, *Medical Imaging Signals and Systems*. Pearson, 2015. [Online]. Available: <https://books.google.com.pe/books?id=HHrangEACAAJ>
- [59] T. L. Szabo and P. Kaczkowski, *Essentials of Ultrasound Imaging*. Elsevier, 2023.
- [60] B. E. Treeby and B. T. Cox, “k-Wave: Matlab toolbox for the simulation and reconstruction of photoacoustic wave fields,” *Journal of biomedical optics*, vol. 15, no. 2, pp. 021 314–021 314, 2010.

- [61] H. J. Kang, M. A. L. Bell, X. Guo, and E. M. Boctor, "Spatial angular compounding of photoacoustic images," *IEEE transactions on medical imaging*, vol. 35, no. 8, pp. 1845–1855, 2016.
- [62] R. J. Lavarello, J. R. Sanchez, and M. L. Oelze, "Improving the quality of QUS imaging using full angular spatial compounding," in *2008 IEEE Ultrasonics Symposium*. IEEE, 2008, pp. 32–35.
- [63] C. Hansen, N. Hüttebräuker, M. Hollenhorst, A. Schasse, L. Heuser, G. Schulte-Altdorneburg, and H. Ermert, "An automated system for full angle spatial compounding in ultrasound breast imaging," in *4th European Conference of the International Federation for Medical and Biological Engineering: ECIFMBE 2008 23–27 November 2008 Antwerp, Belgium*. Springer, 2009, pp. 541–545.
- [64] D. M. Nguyen, T. S. Tran, N. T. Nguyen, T. N. Le, D. H. Nguyen, and T.-T. Nguyen, "Breast anthropometry in vietnamese youth: a comprehensive study of 128 women," *European Journal of Plastic Surgery*, vol. 46, no. 6, pp. 1049–1058, 2023.
- [65] A. Demiröz, A. Türkmen, T. F. Yıldız, and B. Dağhan, "Anthropometric breast measurements of young women with no history of pregnancy or surgery in Turkey," *Journal of plastic surgery and hand surgery*, vol. 55, no. 1, pp. 13–16, 2021.
- [66] M. M. Al-Qattan, S. S. Aldakhil, T. S. Al-Hassan, and A. Al-Qahtani, "Anthropometric breast measurement: analysis of the average breast in young nulliparous saudi female population," *Plastic and Reconstructive Surgery–Global Open*, vol. 7, no. 8, p. e2326, 2019.
- [67] D. K. Avşar, A. C. Aygıt, E. Benlier, H. Top, and O. Taşkinalp, "Anthropometric breast measurement: a study of 385 Turkish female students," *Aesthetic Surgery Journal*, vol. 30, no. 1, pp. 44–50, 2010.

- [68] B. Longo, A. Farcomeni, G. Ferri, A. Campanale, M. Sorotos, and F. Santanelli, “The BREAST-V: a unifying predictive formula for volume assessment in small, medium, and large breasts,” *Plastic and Reconstructive Surgery*, vol. 132, no. 1, pp. 1e–7e, 2013.
- [69] P. Rodríguez and B. Wohlberg, “Efficient minimization method for a generalized total variation functional,” *IEEE Transactions on Image Processing*, vol. 18, no. 2, pp. 322–332, 2008.

